Journal of Geophysical Research: Planets

RESEARCH ARTICLE
10.1029/2017JE005446

Key Points:
- We mapped 2,728 Orientale basin secondary craters (diameter ≈2–27 km) within 6 radii from the Orientale rim crest
- The spatial distribution of secondaries indicates that the Orientale impactor approached from the 60° to 85° azimuth direction with an incidence angle >20°
- The largest Orientale basin ejecta fragment size decreases with increasing distance and fragments diameters in 0.5–2 km are dominant in the investigated area

Supporting Information:
- Supporting Information S1
- Table S1
- Table S2
- Table S3
- Table S4

Correspondence to:
J. Liu and J. W. Head III,
liujianzhong@mail.gyig.ac.cn;
james_head@brown.edu

Citation:
Guo, D., Liu, J., Head, J. W., III, & Kreslavsky, M. A. (2018). Lunar Orientale impact basin secondary craters: Spatial distribution, size-frequency distribution, and estimation of fragment size. *Journal of Geophysical Research: Planets*, *123*, 1344–1367. https://doi.org/10.1029/2017JE005446

Received 21 SEP 2017
Accepted 8 MAY 2018
Accepted article online 17 MAY 2018
Published online 5 JUN 2018

Lunar Orientale Impact Basin Secondary Craters: Spatial Distribution, Size-Frequency Distribution, and Estimation of Fragment Size

Dijun Guo[1,2,3], Jianzhong Liu[1], James W. Head III[3], and M. A. Kreslavsky[4]

[1]Center for Lunar and Planetary Sciences, Institute of Geochemistry, Chinese Academy of Sciences, Guiyang, China, [2]University of Chinese Academy of Sciences, Beijing, China, [3]Department of Earth, Environmental and Planetary Sciences, Brown University, Providence, RI, USA, [4]Earth and Planetary Sciences, University of California, Santa Cruz, CA, USA

Abstract Secondary impact craters, features created by projectiles ejected from a primary impact, contain important information about the primary cratering event and the nature and distribution of its ejecta. The Orientale impact basin (D ~ 930 km) is the youngest and the least degraded large impact basin on the Moon and has the most recognizable secondary impact craters. We identified and mapped 2,728 secondary craters in the investigated area of ~1.66×10^7 km^2, covering an area from the rim of Orientale to six radii. Secondary crater diameters range from ~2 to 27 km, and the median diameter decreases as distance increases. Secondary craters are concentrated predominantly in the northwest and southwest. The ejecta deposit pattern inferred from secondary crater distribution suggests that the Orientale basin was formed by an oblique impact in which the downrange direction was 240°–265° in azimuth, and the incidence angle was steeper than 20°. The cumulative size-frequency distribution of mapped secondary craters steepens as diameter increases and is very well approximated with a Weibull distribution with an exponent 1.32. A widely used crater scaling relationship predicts that the fragments that produced the secondary craters were predominantly in ~0.5–2-km diameter range over the investigated area; the diameter of the largest fragment, however, decreases with increasing distance from Orientale. On the basis of the diameter of the largest secondary crater of Orientale, and other craters and basins, the largest secondary crater of the South Pole-Aitken basin is estimated to be ~40 km in diameter. We explore the implications of these findings for the evolution of the megaregolith and future sample return missions.

1. Introduction

Secondary craters (or secondaries) are the craters formed by impact of ejected fragments from a primary impact crater (Melosh, 1989). According to their type of occurrence and distance from the parent crater, secondary craters can be categorized into four groups (Xiao, 2016): (1) self-secondaries that are produced on the top of continuous ejecta deposits (Shoemaker et al., 1969); (2) near-field secondaries that occur in chains and clusters (Schultz & Singer, 1980; Xiao et al., 2014); (3) distant secondaries (i.e., far-field secondaries) that occur over about 5 radii from the rim of the parent crater, and the craters are more dispersed in spatial than the proximal secondaries (Melosh, 1989; Quantin et al., 2016); and (4) background secondaries: these refer to the distant secondaries that occur in isolated form and are almost indistinguishable from same-sized primary craters (Shoemaker, 1965). As shown in Figure 1, the field of emplaced secondaries is divided into (1) the *self-secondaries facies*, (2) the *continuous secondary facies*, where near-field secondaries are produced; and (3) the *discontinuous secondaries facies* where distant secondaries are formed (Schultz & Singer, 1980; Xiao, 2016; Xiao et al., 2014).

Secondary craters occupy a considerable percentage of the small crater population on planets and satellites. On Europa, secondary craters comprise about 95% of the small craters (diameters less than 1 km; Bierhaus et al., 2005); on Mars, secondary craters are more numerous than primary craters for diameters as large as 9 km (Robbins & Hynek, 2014). Wilhelms et al. (1978) pointed out that in their study area secondaries of the Orientale basin and the Imbrium basin outnumbered primaries in crater sizes smaller than 20 km. Impact crater size-frequency distributions (CSFDs) are a widely used method in determining the ages of planetary surfaces (e.g., Arvidson et al., 1979; Hartmann, 1970; Ivanov et al., 2001; McGill, 1977; Michael & Neukum, 2010; Neukum et al., 1975, 2001). However, the abundance of small secondaries, and the difficulty in distinguishing background secondaries and self-secondaries from small primaries, often leads to considerable uncertainty in

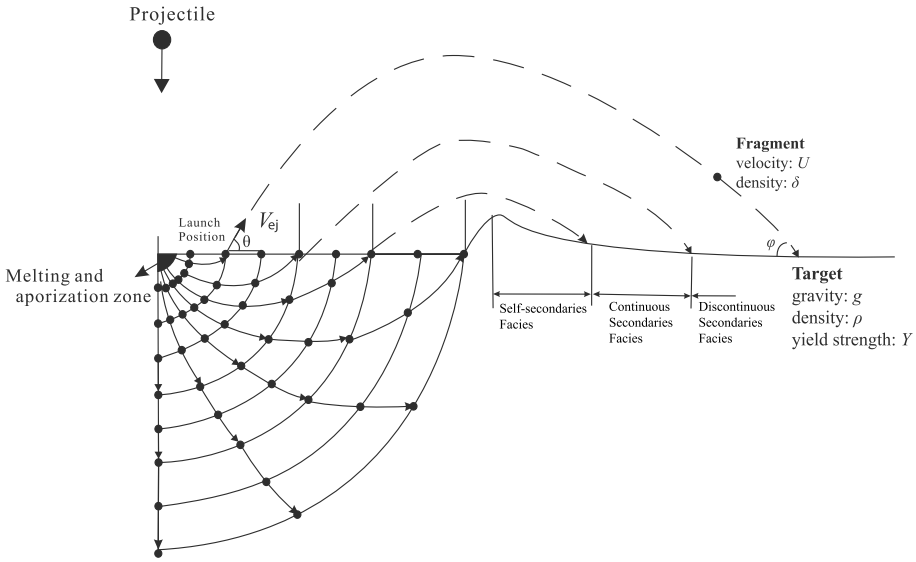

Figure 1. Schematic illustration of the impact excavation processes showing the motion of particles in the excavation cavity, and the resulting ejecta deposit and secondary crater field. Figure is based on Xiao et al. (2014). The parameters: θ = ejection angle, V_{ej} = the ejection velocity, U = secondary impact velocity, δ = the projectile density, g_{moon} = the lunar surface gravity, ρ = target density, and Y = target yield strength.

model ages obtained by the CSFD method. Avoiding the contamination of secondaries has always been a critical issue in using a CSFD to constrain the crater model age of a geologic unit (McEwen & Bierhaus, 2006; Robbins & Hynek, 2011; Strom et al., 2015; Xiao et al., 2014; Xiao & Strom, 2012). Knowledge of the secondary crater population characteristics of secondary crater populations is helpful in the identification of secondary craters, and hence, in improving the accuracy of dating results.

The study of secondary craters also provides an approach to understand the nature of their parent impact crater. The spatial distribution of secondaries is representative of the ejecta distribution, from which the initial primary impact geometry, such as projectile approach azimuth and angle to the surface can be estimated (Anderson et al., 2003; Bottke et al., 2000; Davison et al., 2011; Gault & Wedekind, 1978; Herrick & Hessen, 2006; Pierazzo & Melosh, 2000; Schultz et al., 2007; Shuvalov, 2011; Yamamoto, 2002). In addition, the distinctive characteristics of secondary craters make them more readily recognizable than the thin and discontinuous ejecta deposits over broad distal areas. The thickness and volume distribution of the ejecta deposit in the continuous deposits of the Orientale basin have been estimated (Fassett et al., 2011; Potter et al., 2013; Spudis et al., 1984; Xie & Zhu, 2016; Zhu et al., 2015). However, it is much more difficult to identify them in the more distal discontinuous facies. The spatial analysis of secondary craters formed by ejected fragments provides information about how the ejecta from the parent crater was distributed and the size of those fragments (Hirase et al., 2004; Hirata & Nakamura, 2006; Vickery, 1986, 1987).

The secondary craters of the Orientale basin have been regarded as one of the facies of the Hevelius Formation (McCauley, 1977; Moore et al., 1974; Morse et al., 2018; Scott & McCauley, 1977) and were identified and mapped on a geologic map (1: 5,000,000 scale; Scott & McCauley, 1977) and more recently on an Orientale ejecta map (Morse et al., 2018). Utilizing telescopic data and Lunar Orbiter images, Wilhelms et al. (1978) identified 569 Orientale secondary craters in an area of 1.751×10^6 km^2. The maximum secondary crater diameter is typically estimated to be $<$5% of the parent primary (Bierhaus et al., 2001; McEwen & Bierhaus, 2006; Schultz & Singer, 1980; Shoemaker, 1965). The largest Orientale secondary craters were observed to be more than 20–25 km in diameter (Head et al., 1993; Wilhelms et al., 1978), which is 2.2–2.7% of the Orientale rim diameter or 5.1–6.4% of the 390 km Orientale transient crater diameter as suggested by Johnson et al. (2016). Zhou et al. (2015) systematically studied the circularity of more than 2,100 recognizable secondaries of the Orientale basin. Despite the number of previous studies, comprehensive investigations of Orientale secondaries in an area of all azimuthal range and greater radial distances has not yet been undertaken. The more complete mapping and understanding of the distribution of

secondaries as a function of radial distance and azimuth angle, their size-frequency distribution (SFD), and the ejected fragments size and distribution, can provide additional perspectives to study the formation of Orientale, and is the major goal of this analysis.

As the youngest large lunar basin (Wilhelms et al., 1987), the Orientale basin has the least degraded and most well-preserved interior structure, ejecta facies, and secondary crater fields among basins of comparable scale (Fassett et al., 2011; Head et al., 1993). The Orientale impact basin interior and proximal ejecta deposits currently serve as a paradigm for the interpretation of other basins, and the nature of distal ejecta and secondary crater fields can extend this paradigm further. The nature and size of Orientale basin secondaries is an important constraint to infer secondary crater distributions and sizes of older basins, such as South Pole-Aitken (SPA), whose secondaries have been highly degraded and have yet to be recognized directly. In this analysis, we pursue this goal by mapping the secondary crater field of the Orientale impact basin and assess the population for insights into the nature of the primary impact and the application of these results to recognition of secondary crater fields on older impact basins, their influence on the CSFD used for dating and for the emplacement and sampling of ejecta in future sample return missions.

2. Background of Investigation Area

It is widely accepted that the Orientale basin has four morphologic rings, the Cordillera ring about 930 km in diameter, the Outer Rook ring about 620 km in diameter, the Inner Rook ring about 480 km in diameter, and Innermost ring about 320 km in diameter (Fassett et al., 2011; Head, 1974; Head et al., 1993; Scott & McCauley, 1977; Spudis et al., 1984; Whitten et al., 2011). The fifth ring about 1,300 km in diameter was postulated by some early researchers (Hartmann & Kuiper, 1962; Hartmann & Wood, 1971), but it was poorly defined even if it exists (Moore et al., 1974). There have been controversies about whether the Outer Rook ring (Fassett et al., 2011; Head, 1974; Spudis et al., 1984) or the Inner Rook ring (Xie & Zhu, 2016) is more representative of the position of the transient cavity. The latest study based on high-resolution gravity data from Gravity Recovery and Interior Laboratory (GRAIL) and hydrocode simulation has concluded that the transient crater was ~390 km in diameter but was not maintained because of the subsequent gravitation collapse (Johnson et al., 2016). The innermost part of Orientale basin contains later mare regions, which have a wide age range from ~1.66 to ~3.70 Ga (Whitten et al., 2011). In addition to the mare material, three geologic units associated with the Orientale basin are defined and included in the Orientale Group in the geologic map of the west side of the Moon (Scott & McCauley, 1977). The Hevelius Formation, which occurs beyond the Cordillera Mountains, is the major ejecta deposit of Orientale basin. The Montes Rook Formation lies between the Inner Rook ring and Cordillera Mountains and is interpreted as deposits that were initially similar to the radially textured Hevelius but were modified texturally by late or postbasin megaterrace formation (Head, 1974; Head, 1977). The Maunder Formation is confined to within the Outer Rook ring and represents impact melt emplaced during the terminal modification phase of the Orientale impact event (Head, 1974; Head et al., 1993; McCauley, 1977; Moore et al., 1974; Scott & McCauley, 1977; Spudis et al., 1984; Vaughan et al., 2013).

The investigation of Orientale secondary craters was conducted in an area beginning at the Cordillera ring (the innermost point of easily recognizable Orientale ejecta) and extending out to a radial distance of 6 R (R is Orientale radius) from the Orientale basin rim crest, that is, the Cordillera ring. The study area comprises about 63% of the entire lunar surface area, broader than a lunar hemisphere. Prior to the formation of the Orientale basin and emplacement of the ejecta and secondaries, the study area had been bombarded by numerous impactors, creating craters and large basins (Figure 2). Most of the basins are dated as pre-Nectarian age (Wilhelms et al., 1987) and may be due to a period of Late Heavy Bombardment (Mottmann, 1977; Tera et al., 1974). Among the three Imbrian-aged basins, Orientale marks the latest large-scale impact and produced secondary craters that are recognizable at significant distances from the parent crater. However, the very broad distribution of post-Orientale extrusive volcanism (Head & Wilson, 2017; Wilson & Head, 2017) on the eastern nearside (20°–120° azimuth east of the center of Orientale) profoundly influenced the earlier geologic units by partly or fully filling, embaying or burying them. Indeed, mare volcanism in these regions had begun prior to the formation of Orientale as seen in the distribution of cryptomaria to the south and southeast of Orientale that were subsequently buried by Orientale ejecta (Mustard & Head, 1996; Whitten & Head, 2015). In the mare region, secondary craters created simultaneously with the Orientale event are buried as well, resulting in abrupt decrease in secondary crater density in this direction. One of the goals of the

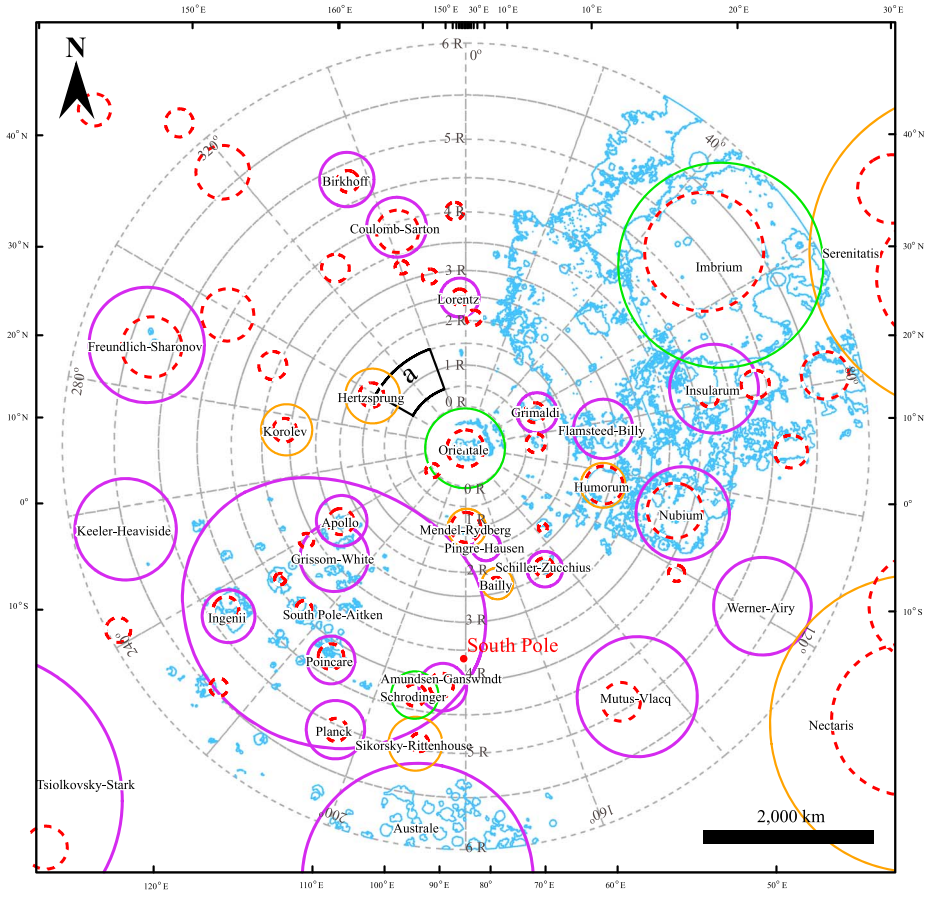

Figure 2. Sketch map shows the geologic setting of the area for the Orientale secondary crater investigation. The solid circles depict the main ring of basins with the age of pre-Nectarian (purple), Nectarian (orange), and Imbrian (green). The data are from Wilhelms et al. (1987) except South Pole-Aitken basin, whose center and outer ring are taken from Garrick-Bethell and Zuber (2009). The dashed red circles represent the Bouguer anomaly revealed by Neumann et al. (2015). Solid line in light blue marks the boundary of mare region provided by Lunar Reconnaissance Orbiter Camera (http://wms.lroc.asu.edu/lroc/view_rdr/SHAPEFILE_LUNAR_MARE). Dashed gray line shows the area where the detailed secondary crater investigation is performed and the annular sectors for secondary crater analysis with respect to different azimuth and distance from the Orientale rim crest. Each annular sector is a half-Orientale radius wide in radial direction and 20 azimuthal degree wide in an azimuthal direction. The sector in the black solid line, marked with "a," is the area of Figure 3 which demonstrates the transition from continuous ejecta deposits to continuous secondaries facies. The map is in stereographic auxiliary projection centered at the center of Orientale (95°W, 19°S). The figures in this paper use the same projection when presenting the entire investigation area.

study is to assess whether the areas with few-to-no secondaries were caused not only by post event burial but also by the occurrence of a "forbidden zone" with no secondary crater formed seen in some oblique impact scenarios (Herrick & Forsberg-Taylor, 2003; Herrick & Hessen, 2006; Schultz et al., 2007).

The pre-Orientale basins identified (Figure 2) are not homogeneously distributed. They occur predominately in the Orientale-centered azimuthal angle of 80°–260° and are absent in the nearside mare region. It is not clear whether fewer basins were formed in this area or basins existed but have been degraded or buried by post-Orientale processes. The analysis of GRAIL gravity data, however, permitted the assessment of subsurface gravity anomalies, and the discovery of more crater-like gravity anomalies in Oceanus Procellarum and other regions (Evans et al., 2016; Neumann et al., 2015). In our study area, a number of Bouguer anomalies not previously recognized or categorized as impact basins are revealed by Neumann et al. (2015), as shown in Figure 2. One such anomaly, 162 km in diameter, is located in the southwest part of the Monte Cordillera (Figure 2). This Bouguer anomaly is associated with a large topographic depression (Figure 2), indicating a buried ancient basin in this location (Neumann et al., 2015). In the mare area around the Orientale basin (Figure 2), no signature of a buried impact basins has been identified (Neumann et al., 2015). However, the

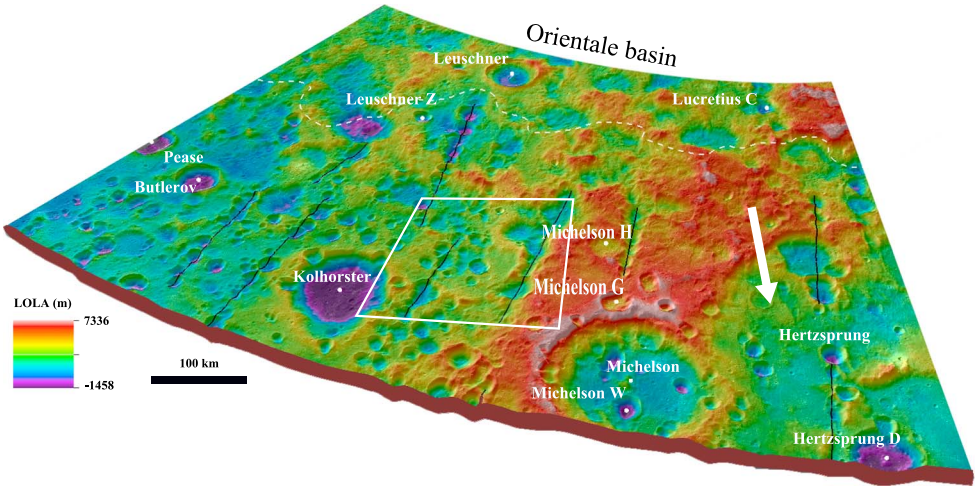

Figure 3. Oblique 3-D view of the topography and morphology of annular sector a in Figure 2. The elevation value is obtained from Lunar Orbiter Laser Altimeter (LOLA) altimetry data. The black lines mark the secondary crater chains. The dashed white line shows the boundary of the continuous ejecta deposits judged from the morphology and images. The white arrow shows the flow direction of ejecta from Orientale basin filling in Nectarian Hertzsprung basin. White dots represent the crater center with the crater name labeled in white. The white quadrangle represents the area of Figure 4. Hertzsprung basin is partly included in the area and its center is out of the image area.

Orientale secondaries, which are smaller in size than basins, would be flooded or buried by the mare if they were formed in the mare region.

In relation to the inner, proximal part of the secondary crater distribution, secondary craters start to occur, mostly in chains, at the edge of continuous ejecta deposit, which is about one radius from the parent crater rim crest (Fassett et al., 2011; McCauley, 1977). The morphology of a transition area (azimuth 300°–340°, distance 0.5–1.5 *R* from Orientale rim) from continuous ejecta deposits to discontinuous ejecta deposits is shown as an oblique 3-D view in Figure 3. In the distal part of the continuous ejecta deposits, a few secondaries appear in chains. The spatial density of secondaries increases beyond the continuous ejecta deposits, so that they occur as compact crater chains (Figure 3). In most cases, craters in a chain overlap (share their boundaries with neighboring craters) in a radial direction. Some of the secondaries are so close to each other that their rims are partly destroyed by the neighbor craters (Figures 3 and 4).

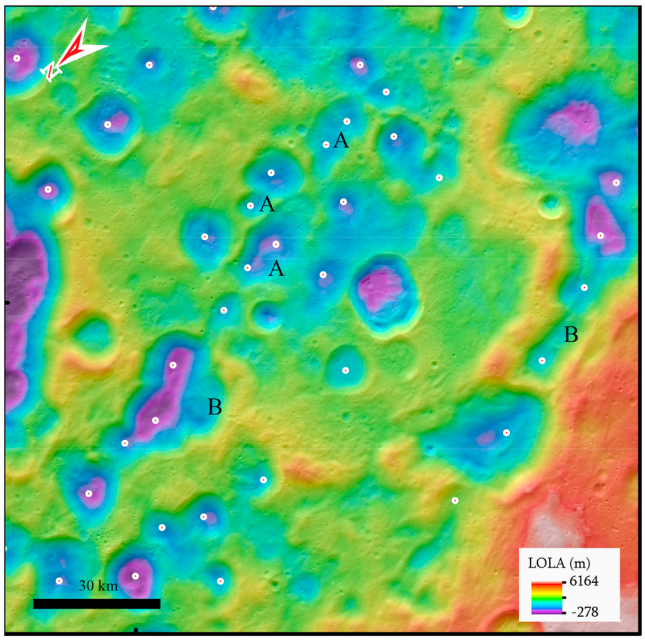

Figure 4. A close view of the secondary craters and crater chains. Red point depicts the identified secondary crater. A: the overlapped crater rim; B: the secondary crater whose diameter is unable to be measured. The extent is shown as a white quadrangle in Figure 3.

The pre-Orientale craters and basins that are located in or at the edge of the continuous ejecta deposits are filled with ejecta from Orientale. For example, the wall of the Nectarian age Hertzsprung basin (Figure 2, azimuth ~300°; 536 km in diameter) is buried and part of the floor is filled by Orientale ejecta (Figure 3). Indeed, for larger pre-Orientale craters and basins, large-scale topographic relief (deep floor and uplifted rim) probably interfered with the flow of ejecta in the near field (Figure 3).

The nature of the target substrate is important because it helps determine the nature and composition of the ejecta from the subsequent Orientale basin, and thus the nature of secondary ejecta fragments (bedrock or megaregolith). The stratigraphy of the Orientale target area consists of an upper crustal megaregolith seen at most areas in the highlands of the Moon, and which is made up of accumulated deposits of ejecta from nearby and distant craters and basins (Petro & Pieters, 2008). One of the most important and earliest contributions to the preimpact topography and stratigraphy of the Orientale region is the ejecta deposit of the South Pole-Aitken basin, primarily emplaced in the southwest portion (Orientale centered azimuth 140°–300°), as shown in Figure 5a. Predicted

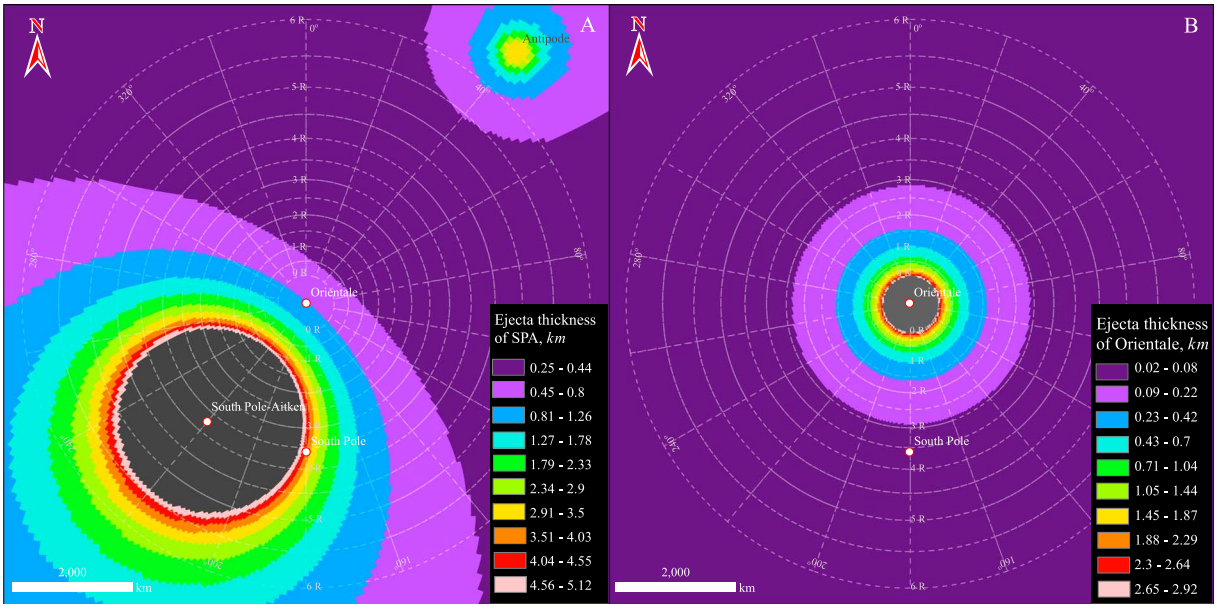

Figure 5. The thickness of ejecta deposits from the South Pole-Aitken (SPA) basin (a) and the Orientale basin (b). The location of the South Pole is shown on both images. Dashed gray lines, with azimuth and distance from Cordillera labeled, outline the current Orientale secondary crater investigation area. Thickness decay model of SPA basin is applied with equation (12) from Pike (1974) by assuming 2400 km diameter given by Garrick-Bethell and Zuber (2009). Note that the thickness surges around the antipode point. Thickness of ejecta deposits from Orientale is estimated using the model from Fassett et al. (2011).

SPA ejecta thicknesses range from 0.25 km in the NE part of the target area, to up to ~1.8 km in the SW part of the target area (Pike, 1974). Most ejecta contributions from other basins are insignificant due to their great distance from Orientale, and the fact that ejecta delivered will be in their distal discontinuous ejecta region, and thus delivered as localized secondary craters, chains, and clusters, as is the case of the distal Orientale ejecta analyzed here. The most prominent basin contributions are likely to come from the Mendel-Rydberg Basin to the south, the Grimaldi basin to the east, and the Hertzprung basin to the west (Figure 2).

After the formation of the SPA basin, more ejecta from pre-Orientale basins was deposited in the investigation area, resulting in a significant thickness of regolith (Petro & Pieters, 2008). In the study area, the SPA ejecta deposits could be ~250-m thick (Figure 5a), and the thinnest ejecta deposits accumulated by post-SPA impacts could be ~100–200 m (Petro & Pieters, 2008). To penetrate a 400-m-thick layer, the crater must be at least 4 km in diameter (Pike, 1972); therefore, some of the large secondaries from Orientale could expose SPA ejecta deposits and probably the primary crust, even considering additional ejecta from post-SPA impacts. In comparison to the SPA ejecta, the ejecta from Orientale is much thinner in the area beyond 1.5 radii from Orientale basin (Fassett et al., 2011), as shown in Figure 5. Orientale ejecta deposits are about 2.9-km thick at the Cordillera ring but decay to less than 500 m on average at one radius from the Orientale rim, the approximate boundary of continuous ejecta deposits (Figure 5b).

3. Data and Method

3.1. Data

The identification of secondary craters is based primarily on the examination of 100 m/pixel LROC (Lunar Reconnaissance Orbiter Camera) wide-angle camera images (Robinson et al., 2010), combined with 1,024 pixel per degree Lunar Orbiter Laser Altimeter topography data (Smith et al., 2010). In areas where significant topographic undulations make it difficult to identify and measure secondary craters, the 7 m/pixel terrain camera (TC) image and the derived topography data from SELENE (Selenological and Engineering Explorer) mission are applied (Haruyama et al., 2008).

3.2. Secondary Crater Identification

Typical secondary craters and primary craters are distinct in many aspects (Pike & Wilhelms, 1978; Robbins & Hynek, 2014; Shoemaker, 1962; Wilhelms, 1976; Wilhelms et al., 1978). Considering the large size of the

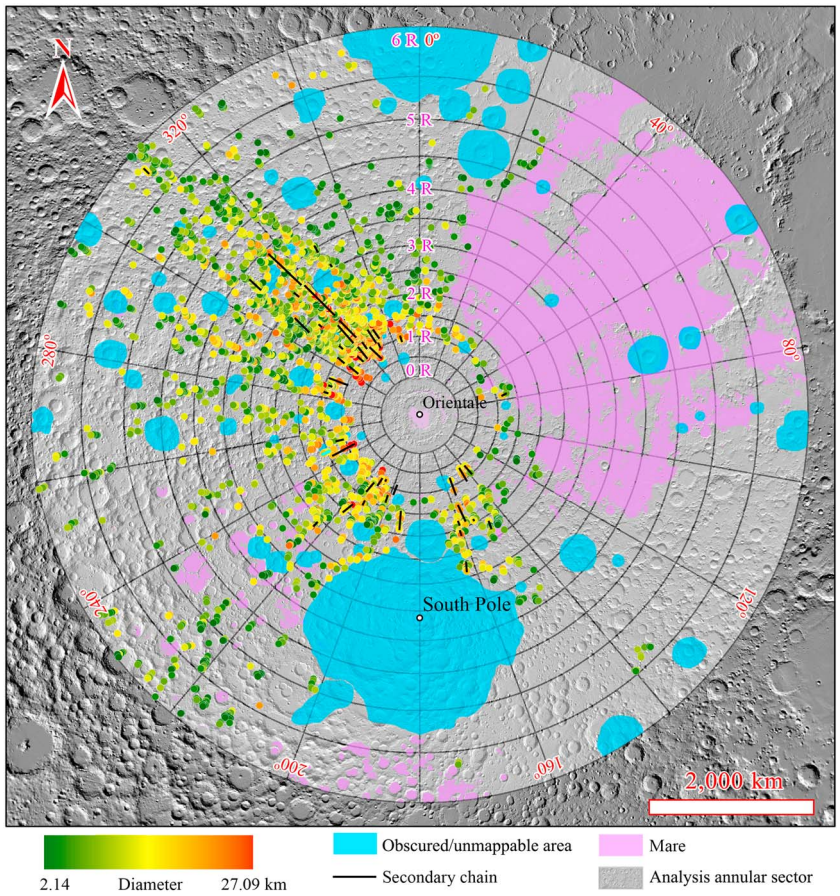

Figure 6. Locations of 2,728 Orientale secondary craters identified in this analysis. Red indicates largest diameters, and green represents lowest diameters. Secondary chains are marked with short black lines radial to Orientale. The purple area designates post-Orientale mare deposits. Light blue denotes post-Orientale impacts and the area surrounding the south polar region where illumination geometry results in poor detectability. The base map is a hillshade image from Lunar Orbiter Laser Altimeter elevation data. In later figures, the mare region and obscured/unmappable areas are mapped using these same symbols if not specified.

Orientale basin, its secondary craters can be recognized on the basis of six criteria: (1) entrained within an elongate, chain-like crater group radial to the Orientale basin; (2) occurs in a cluster of craters of similar diameter and in broad spatial association with, and typically distal to, crater chains; (3) individual craters, clusters or chains are characterized by a "herringbone" ejecta pattern with herringbone v-shape point back toward Orientale; (4) has an elliptical shape with its long axis radial to the Orientale basin center; (5) shows interference features such as septa and mounds; and (6) generally displays shallower rim-to-floor depth than primary impact craters.

The investigation area of analysis is further divided into 12 subannuli, each with a width of half *R*, to compare the craters at different radial distance in more detail. The subannuli are additionally divided into 20 azimuthal degree-wide sectors (Figures 2 and 6). In the next stage of the analysis, a grid is formed to analyze secondaries in consecutive specific sectors, each with a different radial distance and azimuth; this systematic approach of searching for secondaries sector by sector helps to avoid the omission of secondaries that might occur if they were searched for in a more random fashion.

Three factors limit the complete radial and circumferential assessment of the distribution and nature of Orientale secondary craters. (1) Subsequent to the emplacement of the Orientale ejecta deposits, many large impact craters (e.g., Butlerov crater in Figure 3) were formed by the general projectile flux and these have subdued, destroyed, or buried Orientale secondaries in some specific areas. (2) Post-Orientale mare basalt emplacement has buried a broad area in the east side of the Orientale basin, implying that it is difficult to

impossible to recognize secondary craters and ejecta deposits there. (3) Solar illumination conditions severely inhibit the ability for precise recognition of secondary craters in the polar region in some areas. These three types of areas are excluded from our analysis (see Figure 6). On the basis of image data resolution and post-Orientale crater degradation processes, we are unable to confidently identify and characterize secondary craters with diameters less than ~2 km.

The secondary craters recognized are mapped, and their diameters measured, using Crater Helper Tools from the USGS (https://astrogeology.usgs.gov/facilities/mrctr/gis-tools). The shapes of secondary craters are often very elliptical or deformed. In measuring the crater diameter, we adopt the minor axis if the shape is elliptical. For the craters that are very round, only when they are formed as chains or clusters radial to Orientale are they identified as secondary craters. Craters that may be secondaries of the Orientale basin but have unmeasurable diameters (too indistinct or degraded) are excluded from the catalog; such craters are small in number and distributed over almost all of the study area, so their exclusion does not cause significant biases in our analysis.

To guarantee that the secondary crater catalog is as reliable as possible, crater identification and diameter assessments were checked three times before performing further analysis. The most reliable identification and mapping is generally closer to the primary crater, and we consider that the secondaries identified within four (4) radii from the Orientale rim crest are very reliable. In this area, the number of secondary craters identified is 2,065. On the basis of the difficulty in distinguishing secondary from primary craters located at great distances from the point of impact, there may exist a small number of craters in the catalog that are actually primary craters and alternatively, some craters excluded from the catalog may be secondaries. Nevertheless, the catalog can provide credible first-order results when analyzing the overall population characteristics and even more reliable results if the analysis is based on craters proximal to (within four radii) the Orientale basin rim crest.

3.3. Crater Ejecta Scaling Law

We use crater ejecta scaling laws to estimate the properties of the ejected fragments that formed the measured secondaries. First, the ejection velocity of ejected fragment can be estimated based on the distance of the secondary crater from primary crater, r (Vickery, 1986). On the Moon, the relation of half-angular distance of travel (θ), ejection velocity (V_{ej}), and ejection angle (θ) can be expressed as

$$\tan\phi = \left(V_{ej}^2 \sin\theta \cos\theta\right) / \left(gR_{\text{moon}} - V_{ej}^2 (\cos\theta)^2\right) \tag{1}$$

$$\phi = r/(2R_{\text{moon}}) \tag{2}$$

where R_{moon} and g are the lunar radius and surface gravity, respectively (Vickery, 1986). Hence, the ejection velocity can be calculated through

$$V_{ej} = \frac{\sqrt{gR_{\text{moon}} \tan(r/2R_{\text{moon}})}}{\sqrt{\tan(r/2R_{\text{moon}})(\cos\theta)^2 + \sin\theta\cos\theta}} \tag{3}$$

Because the atmospheric drag on the Moon is negligible, we can assume that impact velocity of fragment equals its ejection velocity (V_{ej}; Hirata & Nakamura, 2006; Vickery, 1986), so assuming a known ejection angle θ, the impact velocity of secondaries can be computed with equation (3).

Derivation from the scaling relationships of Holsapple (1993) and Holsapple and Housen (2007) provided the general form of the scaling relationship:

$$\frac{R}{a} = K_1 \left[\frac{ga}{U^2} \left(\frac{\rho}{\delta}\right)^{\frac{2\nu}{\mu}} + \left(\frac{Y}{\rho U^2}\right)^{\frac{2+\mu}{2}} \left(\frac{\rho}{\delta}\right)^{\frac{\nu(2+\mu)}{\mu}} \right]^{-\frac{\mu}{2+\mu}} \tag{4}$$

where a, U, δ, and m are the impactor radius, normal velocity component, density and mass, g is the gravitational acceleration, ρ and Y are the density and strength of the target material, R is the final crater radius, K_1 is experimentally derived properties of the target material, μ and ν are two scaling exponents. In this study, the values of the parameters are assigned as k_1 = 1.03, μ = 0.41, and υ = 0.4 (e.g., Holsapple, 1993;

Table 1
Statistics of Identified Orientale Secondary Craters

Parameter	Value
Count	2,728
Mean (km)	8.47
Standard deviation (km)	4.11
Minimum (km)	2.14
25th percentile (km)	5.48
Median (km)	7.52
75th percentile (km)	10.53
Maximum (km)	27.09

Holsapple & Housen, 2007); ρ = 2,550 km/m^3, δ = 3,000 km/m^3 (e.g., Huang & Wieczorek, 2012; Wieczorek et al., 2013); and Y = 1.0 MPa (e.g., van der Bogert et al., 2017).

If the effect of strength is much smaller than gravity in cratering, that is, if it takes much more energy to loft the material out of the crater bowl than it takes to effectively break the material apart, the cratering is gravity dominated. In this scenario, equation (4) can be simplified as

$$\frac{R}{a} = K_1 \left[\frac{ga}{U^2} \left(\frac{\rho}{\delta} \right)^{\frac{2\nu}{\mu}} \right]^{-\frac{\mu}{2+\mu}} \tag{5}$$

The impactor radius a can be expressed as

$$a = \left(\frac{R}{K_1} \right)^{\frac{2+\mu}{2}} \left(\frac{g}{U^2} \right)^{\frac{\mu}{2}} \left(\frac{\rho}{\delta} \right)^{\nu} \tag{6}$$

4. Results

4.1. Secondary Craters

On the basis of the criteria previously described, we identified a total of 2,728 secondary craters in the study area of ~1.66×10^7 km^2 (Figure 6). They exhibit a diameter (D) range from 2.14 to 27.09 km (Table 1). The maximum secondary crater diameter mapped (~27 km) is approximately 3% of diameter of the Orientale basin Cordillera Ring, which is within the range of secondary-primary diameter ratio of craters on the Earth, Moon, Mars, Mercury, and Europa (McEwen & Bierhaus, 2006; Schultz & Singer, 1980).

It is obvious that the secondaries are not evenly distributed in the study area, but rather are very heterogeneously distributed. Specifically, excluding the region beyond 1.5 R from Orientale rim where the east side was flooded by mare basalts, the northwest quadrant of the Orientale basin exterior has the most concentrated secondaries, while the density in the rest of the exterior is significantly lower, especially on the eastern side (Figure 6). As shown in the diameter color coding of Figure 6, the high crater densities in the highland terrain are dominated by the concentration of Orientale secondary craters in the 9–16 km diameter range, which is consistent with estimations of Povilaitis et al. (2017) and van der Bogert et al. (2017).

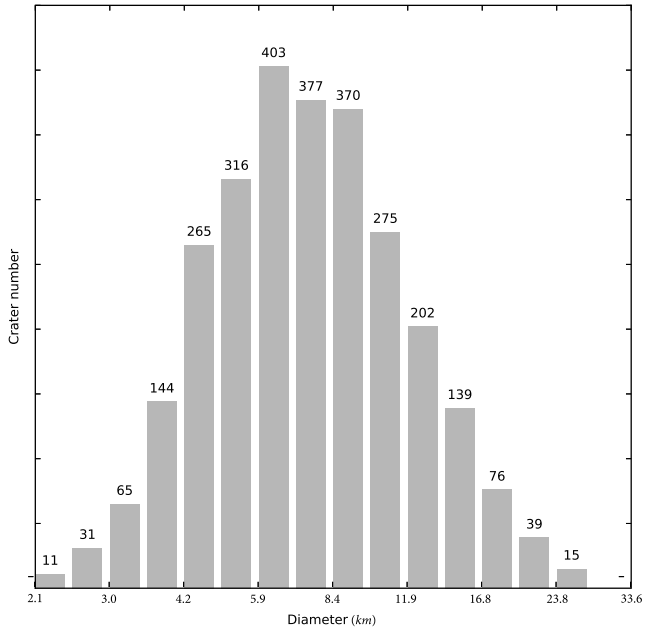

Figure 7. Histogram of the diameter distribution of Orientale secondary craters. The bin widths are geometric diameter values as suggested by Arvidson et al. (1979). The geometric scale of bins in this figure is fourth root of 2, and the leftmost edge represents the smallest diameter, 2.1 km.

The Orientale secondary crater size distribution histogram of craters identified in this analysis is shown in Figure 7. The mean and median diameters are 8.47 and 7.52 km, respectively (Table 1), and craters with diameter from ~4 to ~12 km have the highest frequency. They have a total number of 2,150 and occupy 78.8% of the total populations. Crater number increases with increasing diameter until 5.9 km, after which crater number decreases. The lower number of craters smaller than 6 km is probably due to the fact they are not completely mapped. According to studies about distinguishing secondary craters from fresher primary craters (Hirata & Nakamura, 2006; Robbins & Hynek, 2011, 2014; Xiao, 2016; Xiao et al., 2014), more small size secondary craters should be formed in the cratering process of the Orientale basin. However, smaller craters are more easily degraded by postevent processes than larger ones. On the other hand, it is difficult to identify and distinguish smaller secondary and primary craters because they have similar shapes and are more easily obscured.

4.2. Secondary Chains

On the basis of the alignment pattern of secondary craters, 47 secondary chains were identified in the mapped Orientale panels as shown in Figure 6. Generally, secondary chains occur in regions where secondary craters are relatively higher in density. The azimuth and distance range of secondary chains from the Orientale rim crest are shown in Figure 8.

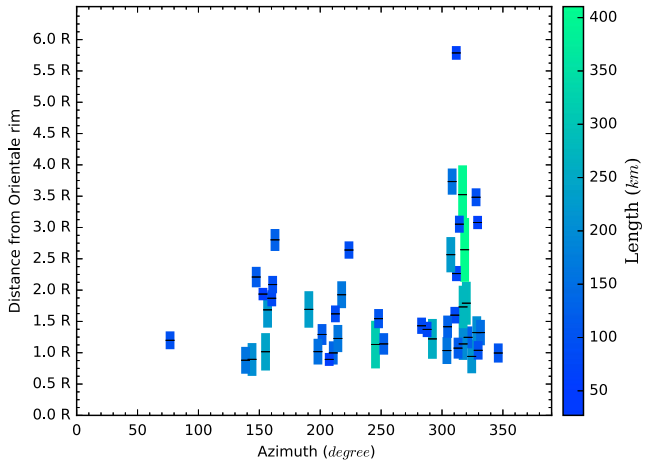

Figure 8. Distribution of secondary chains with respect to the azimuth angle and distance from the Orientale rim crest. The beginning and end of each vertical bar are corresponding to their locations on the chain. The azimuth is measured from the middle point of the chain to Orientale center. The distance is normalized to the Orientale basin radius, *R*. The deeper green bars represent longer chains, while shorter chains are deeper in blue. The horizontal black line on a bar marks its middle point.

The length of secondary chains ranges from 27 to 410 km, with a median value of 101 km and averagely 128.7 km. There are two distinctly longer chains at an azimuth of ~320°; closer to Orientale basin, two shorter chains can be found in this same direction (Figures 6 and 8).

Crater chains are mostly located in the azimuthal sector of 130°–350°, but there is a decline in the sector of 230°–280°, where only three chains are recognized and the density of secondaries in this region is also relatively lower than the nearby area (Figures 6 and 8). This direction corresponds to the downrange direction of the Orientale impact event proposed by several workers (Liu et al., 2016; Morse et al., 2018; Schultz & Papamarcos, 2010). In the azimuth range sector where the mare region is located, only one secondary chain, ~70 km long, is identified, located within 1–1.5 *R* from the Orientale rim crest at the azimuth close to 80° (Figure 8).

From the radial perspective, the secondary chains are mainly located in the annulus that lies 0.5 *R* to 4 *R* from the Orientale rim crest but concentrated in the distance range of 0.5–2 *R*, where secondary crater density is higher on average (Figures 6, 8, and 10). One isolated secondary chain (centered at 173.45°E, 43.62°N) that is likely to be related to the Orientale basin is identified at about 5.7 *R*, the farthest from Orientale (Figures 8 and 9). The diameters of the craters are around 11 km, which is much larger than the mean secondary diameter at this distance but in the diameter range (Figure 11). Despite the great distance, its radial direction can be traced back to the Orientale basin, but it is possible that the chain was formed by an impact basin other than Orientale.

5. Spatial Distribution of Secondary Crater

We calculated the mean diameter and density of identified secondaries located in each annular sector and these are shown in Figure 10. A few important observations and correlations are indicated (Figure 10): (1) in general, the closer to the Orientale rim crest, the greater the mean diameter; (2) The variation of secondary crater density with distance is more complicated than mean diameter; (3) within one *R* from the Orientale rim crest, both the mean diameter and the density vary along different azimuthal angles; and (4) As the distance from the Orientale rim crest increases, the mean diameter is very similar in different azimuth sectors located at the same distance (except in the section where the mare basalts are broadly developed), while the secondary crater densities in those sectors have notable discrepancies along different azimuths.

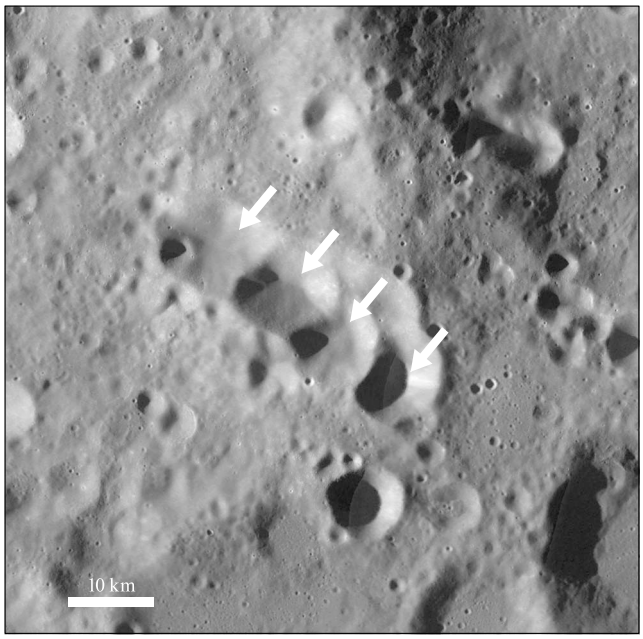

Figure 9. LRO (Lunar Reconnaissance Orbiter) Wide Angle Camera image of the secondary crater chain at ~5.7 *R*. The white arrows point to the craters in the chain.

5.1. Secondary Crater Distribution as a Function of Distance From the Orientale Rim Crest

Because of the variability of fragment size, speed, and incidence angle at different distances from the parent crater, the secondary crater density and diameter vary with distance (e.g., Hirase et al., 2004; Oberbeck, 1975; Xiao, 2016). The distribution of the mean diameters suggests that larger secondaries were formed in the proximal region, while crater density does not follow a linear relationship with distance as diameter does (Figure 11).

5.1.1. Secondary Crater Number and Density as a Function of Distance

The number and density of secondaries in annuli at different distances show the same trend with distance. Both number and density dramatically increase from 1 *R* to 1.5 *R* and then remain relatively stable until 2.5 *R* at which point they rapidly decline. This decreasing trend ceases at the 4–4.5 *R* annulus, beyond which the number and density remain at low values, with small deviations (Figures 11a and 11b). Secondaries are most concentrated in the distance range area from 1 to 3.5 *R*, and the highest

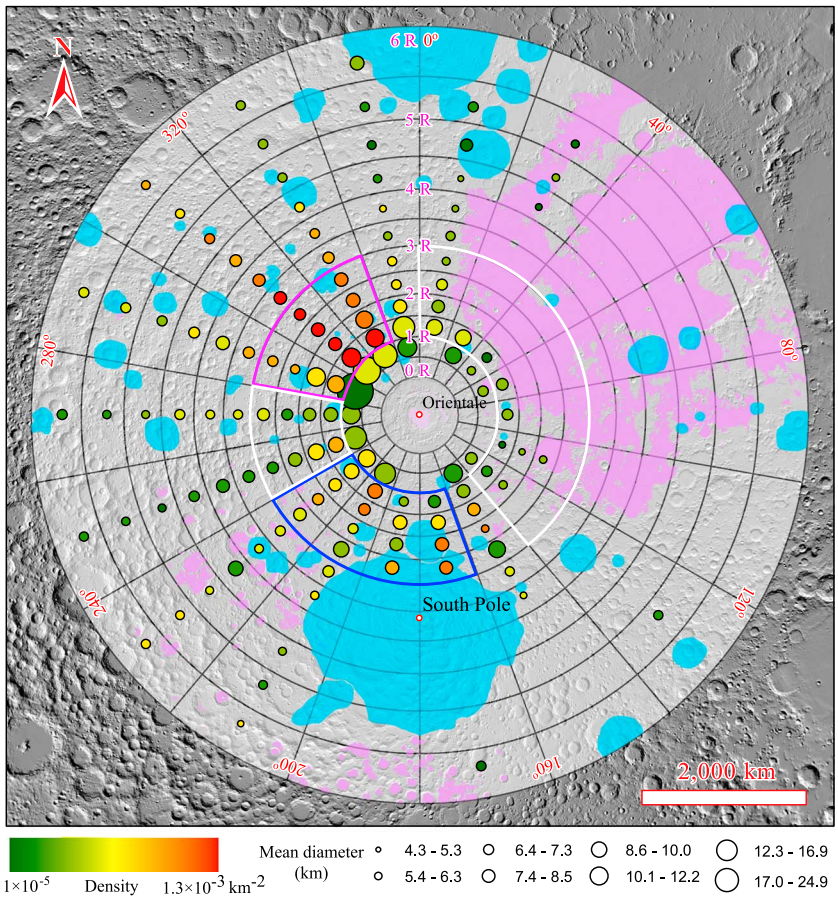

Figure 10. The densities and mean diameters of secondary craters in annular sectors. Within the 1 *R* to 3 *R* radial range, the sector outlined with the purple line is the high-density region; outlined with a blue line is the medium-density area; and outlined with white lines are the low-density regions. The high-density and medium-density regions are approximately bilateral symmetry to the azimuthal angle of about 240°–280°. The area of mare and the obscured/unmappable areas are subtracted when densities are calculated. This process is applied in all the density calculations in this paper.

crater number and highest crater density are both located in the annuli at 1–2.5 *R* (Figures 11a and 11b). Secondary chains and clusters are abundant in the high-density region (Figure 8), corresponding to the "continuous secondaries facies" (Schultz & Singer, 1980; Xiao et al., 2014).

The difficulty in identifying secondary craters in the distal region beyond 4 *R* may be part of the reason for their low crater numbers and densities in this region. In distal areas, secondary craters become more similar

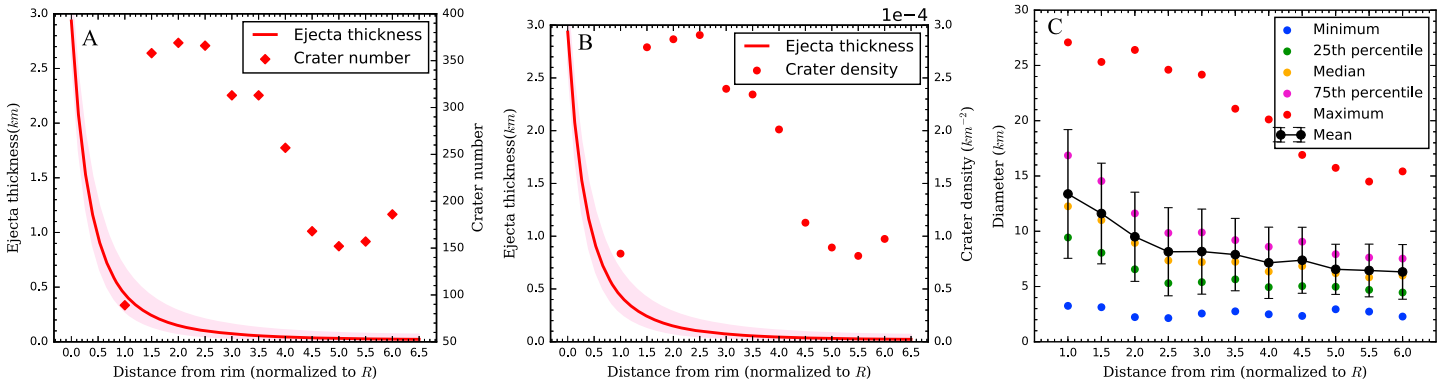

Figure 11. Ejecta thickness and secondary crater number (a) and density (b) versus distance from Orientale rim (Fassett et al., 2011); crater diameter statistics (c) in half *R* width annuli at different distances. The *x* axis represents the outer boundaries of annuli. The pink shadow in (a) and (b) shows the error range. The mean diameter error in (c) is given by the diameter standard deviation.

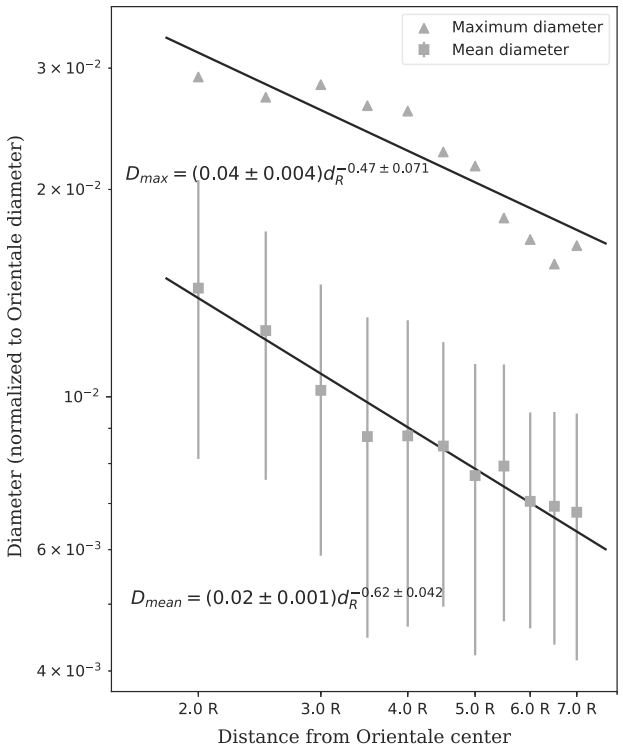

Figure 12. Power law fits of mean and maximum secondary crater diameter in annulus versus distance from Orientale. The distance is measured from the outer boundary of annuli to the Orientale basin center and is normalized to the Orientale radius. The diameters are normalized to the diameter of Orientale basin, and the error bars represent standard deviation.

to small primary craters in rim-to-floor depth and circularity (Robbins & Hynek, 2014; Shoemaker, 1962; Wilhelms, 1976). The patterns of chains and clusters are known to be inconspicuous or to disappear in the discontinuous secondaries facies (Schultz & Singer, 1980; Xiao et al., 2014). On the other hand, the modeled Orientale ejecta thickness decreases to almost zero at radial ranges greater than 4 *R*, as suggested by Fassett et al. (2011; Figures 11a and 11b), indicating that there should be a decline in the overall spatial density of projectiles as well.

We compare the density in smaller sectors that have the same azimuthal range but different distances in Figure 10; the observed variation with distance are consistent with the density variation with distance of all the secondaries in each annulus. However, the inflection points in different azimuth intervals are at different positions due to the asymmetry of the ejecta distribution. Nevertheless, for most azimuthal intervals, the secondary crater densities in sectors of the six radii annulus are relatively stable (Figure 10).

5.1.2. Secondary Crater Diameter as a Function of Distance

As shown in Figure 11c, with increasing distance from the Orientale rim crest, all statistical percentiles except the minimum value of secondary diameters decrease in different annuli, and the minimum diameter is stable at different distances. The maximum diameter decreases gradually with increasing distance, while the mean diameter has distinct slopes before and after an inflection point at 3 *R* (Figure 11c). The slope of the mean diameter decrease with increasing distance is remarkably steeper from the first annulus to the annulus at 2.5–3 *R* than the slop of further distant annuli (Figure 11c). As shown in Figure 12, the best fit of the power law function relating the mean diameter (D_{mean}, normalized to Orientale diameter) to distance from the center of Orientale (d_R, normalized to Orientale radius) is

$$D_{\mathrm{mean}} = (0.02 \pm 0.001) d_R^{\,-0.62 \pm 0.042} \tag{7}$$

and the power law function relating the maximum diameter (D_{max}, normalized to Orientale diameter) to the same normalized distance is

$$D_{\mathrm{max}} = (0.04 \pm 0.004) d_R^{\,-0.47 \pm 0.071} \tag{8}$$

The power law exponents suggest that the log–log slope of the mean diameter (0.62) is slightly larger than the log–log slope of the maximum diameter (0.47) over the entire distance range.

We note that with increasing distance from the Orientale basin, the maximum crater diameter declines while the minimum crater diameter does not change much; hence, the diameter variation of secondaries within each annuli weakens with increasing distance. This phenomenon can be seen from the range of circle size in different sectors as shown in Figure 10, as well as in the standard deviation of diameter in Figure 11c. In the sectors of 0.5–1 *R* annulus in Figure 10, the discrepancy of mean diameters in different sectors is over 4 times: the greatest mean diameter is 24.9 km, but the smallest mean diameter is only 6 km, and there are sectors without secondary craters identified. In comparison, the mean diameter discrepancy in the annulus 1–1.5 *R* is much less; the largest mean diameter is 15.3 km, and the lowest mean diameter is 4.9 km (Figure 10). The change in mean diameter variation with distance indicates that the size of fragments in the ejecta become more and more homogeneous, which is discussed further in section 7.

5.2. Secondary Crater Distribution as a Function of Azimuth

The diameters and densities of secondaries are inhomogeneous with respect to azimuth angles. To illustrate their distribution with regard to azimuth, the average secondary crater diameter and number density are calculated for bins with 5° azimuthal width (Figure 13). The density and average diameter show different relationships with azimuthal direction, which provide clues to the impact trajectory.

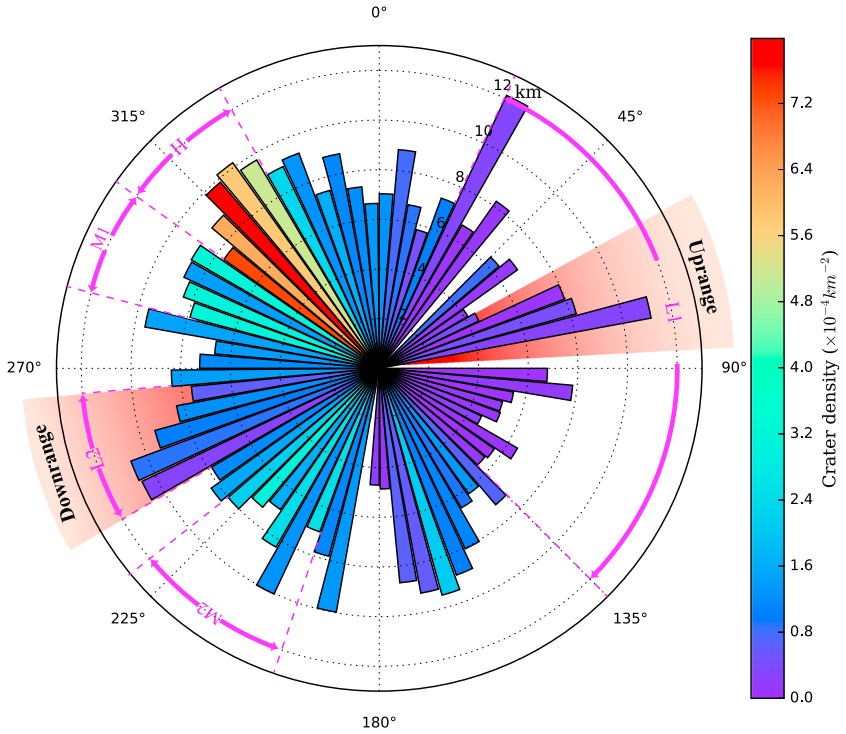

Figure 13. The density and average diameter of Orientale secondary craters located in different azimuthal bins. Each bar represents a 5° azimuthal wide sector within a radial distance of 1–6 *R* from the rim of Orientale. The color of the bar represents the density of secondaries, and the length represents the average diameter. H: high-density region, M1 and M2: medium-density region, and L1 and L2: low-density region. Azimuth range of possible uprange and downrange of Orientale basin impact direction are shown.

5.2.1. Density Distribution as a Function of Azimuth

The density of secondary craters does not show a continuous change with azimuth angle. As shown in Figures 10 and 13, the azimuthal density distribution can be divided into five regions: the northwest high-density region (H) and the adjacent medium-density region (M1), the southwest medium-density region (M2), the wide low-density area (L1) in the east, and the other narrow low-density area (L2) in the west. The high-density sectors are in the region with azimuth from 305° to 330° (Figure 13), which occupies ~6.9% of the entire area but has ~36.9% of the crater populations. Although most of the ejecta deposits on the eastern side are buried under later mare deposits, the sectors that are less than 1.5 *R* from the Orientale rim crest are exposed and available to search for secondary craters. There are very few secondary craters in each of those sectors and none in one sector even though there are no maria or obscured/unmappable areas (Figure 10). This distribution implies that the low density of secondary craters to the east of Orientale basin within 1.5 *R* from the rim was not caused by mare emplacement.

Asymmetrical ejecta distribution caused by low-angle impact has been documented by many studies (e.g., Anderson et al., 2003; Bottke et al., 2000; Davison et al., 2011; Gault & Wedekind, 1978; Herrick & Hessen, 2006; Pierazzo & Melosh, 2000; 500 Schultz et al., 2007; Shuvalov, 2011; Yamamoto, 2002). On the basis of the occurrence of ejecta deposits formed by impacting projectiles approaching the target from different incidence angles, ejecta planforms can be divided into five categories which range from near-vertical to low-angle incidence impact (Figure 14): these are (a) symmetric, (b) offset, (c) offset and concentrated cross range, (d) forbidden zone, and (e) butterfly (Herrick & Forsberg-Taylor, 2003; Herrick & Hessen, 2006). The implied direction of impact is shown in Figure 14. On the Moon, the transition angles of offset (b), forbidden zone (d) and butterfly (e) are interpreted to be about 45°, 25°, and 10°, respectively, but the transition angle of offset and concentrated cross range is unknown (Herrick & Forsberg-Taylor, 2003). Here we examine the asymmetry in the distribution of secondary craters as a proxy for the asymmetry of the ejecta blanket to estimate the impact trajectory direction and angle to the target surface.

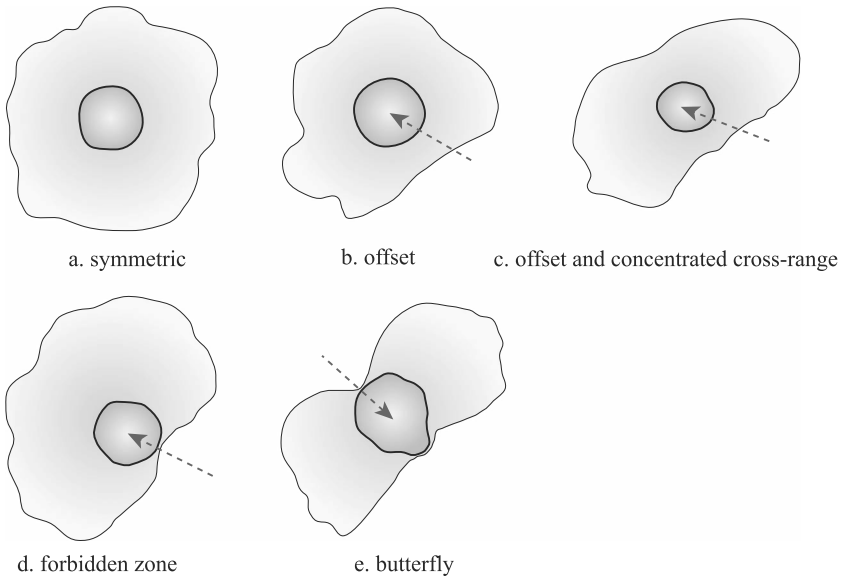

Figure 14. Five ejecta planforms based on Herrick and Forsberg-Taylor (2003) and Herrick and Hessen (2006). From (a) to (e), the impact is from near-vertical to low-incidence angle. The arrow indicates the impact direction.

Comparing the sectors that span a radial distance from 1 *R* to 3 *R* in Figure 10, those with high secondary crater density and with medium density shows a bilateral symmetry distribution centered on an azimuth of 240°–280°. This pattern is between the ejecta planform characteristics of offset and concentrated cross-range (Figure 14c) and forbidden zone (Figure 14d). In the planform of offset and concentrated cross-range (Figure 14c), the major axis of the ejecta ellipse is inferred to be the cross-range direction and the offset direction of the ejecta relative to the crater center is inferred to be the downrange direction (Herrick & Hessen, 2006). If we regard the near-field secondaries as representatives of continuous ejecta deposits (the ejecta fragment diameter and volume calculated from secondaries is discussed in section 7 and shows similar distribution pattern with secondaries), the secondary crater high-density region (H, azimuth between 305° and 330°) and medium-density region (M2, azimuth between 200° and 230°) are approximately symmetric to about 265°azimuth, as shown in Figure 13. Given that the density of region M1 is apparently higher than most of the rest of the regions except for the high-density region, and the existence of a very low density at an azimuth around 240°, the scope of downrange of impact could be down south to 240° because the cross-range direction is generally higher in density than downrange direction for planforms in Figures 14c and 14d. In conclusion, the Orientale impact downrange direction is interpreted to be 240° to 265°; therefore, the uprange direction is interpreted to be 60° to 85° (Figure 13). Our estimate is consistent with previous studies of different features of the Orientale basin such as from ejecta grooves (Schultz & Papamarcos, 2010), central uplift ridge (Liu et al., 2016), and the distribution of ejecta facies (Morse et al., 2018), showing that the incoming bolide trajectory is from northeast to southwest.

Estimating the angle of the impact trajectory to the target surface is less straightforward than the impact azimuth. Using the secondary crater density planform asymmetries as a direct proxy for ejecta deposit asymmetry, the planform of the Orientale ejecta is between (Figure 14c) offset and concentrated cross range and (Figure 14e) forbidden zone. This would imply an incidence angle in the range of 25° to 45° (Herrick & Forsberg-Taylor, 2003). However, while secondary crater density is related to the concentration of ejecta, secondary craters extend much further than the continuous ejecta blanket and are therefore formed by faster ejecta that is ejected from closer to the impact center. Previous studies (e.g., Anderson et al., 2003; Shuvalov, 2011) have shown that faster ejecta, produced at the early time of crater growth, show much greater asymmetry than slower ejecta formed later during crater growth. Therefore, a given planform asymmetry is likely to be observed within secondary crater distributions at a steeper angle of incidence than the corresponding planform asymmetry in the continuous ejecta. This effect is likely to be particularly pronounced in impacts, such as Orientale, that have a low cratering efficiency (ratio of crater size to impactor size). This suggests that the lower limit of the estimated range of 25° to 45° may be underestimated.

An additional constraint on the impact angle can be obtained from consideration of the crater rim planform. Less than 5% of craters 2–90 km in diameter on the lunar mare have an ellipticity (length/width) exceeding 1.2, which suggests an elliptical crater shape threshold angle of about 10° for such craters on the Moon (Bottke et al., 2000). On the other hand, for the larger basins such as Orientale, which have low cratering efficiency, the elliptical rim may occur at steeper angles of incidence (Collins et al., 2011). The 10° increase in elliptical crater threshold angle is a measure of the possible increase in the various ejecta planform threshold angles, which are also derived from lunar craters that are much smaller than Orientale.

To get the ellipticity of Orientale basin, the residuals of Orientale rim crest are selected from Montes Cordillera and used to fit an ellipse (Figure S4). Ellipse fitting suggests that the center is (−95.25°E, −19.95°S), that the semimajor and semiminor axes are 503.74 km and 457.59 km, respectively, and that the rotation is ~44.4° from north direction. The axes lengths indicate the ellipticity of Cordillera ring is ~1.1. The elongation azimuth angle of ellipse does not exactly locate in the azimuth range of proposed impact direction. They have a small difference of about 15° and both of them are in the direction of northeast-southwest. Given that the Montes Cordillera is heavily collapsed especially at the southwest region where only two points are used to constrain the ellipse fitting, the elongation for fitted ellipse does not contradict with the proposed impact direction. Therefore, the ellipticity of Orientale basin is very likely caused by oblique impact. Assuming that the impactor diameter is 64 km and the velocity is 15 km/s (Johnson et al., 2016), with the equations from Collins et al. (2011, Eqs. 1 and 2), the elliptical crater threshold angle for the Orientale basin is estimated as ~20° from the surface. The ellipticities indicate that Orientale is slightly elliptical and therefore would have been produced by an impact trajectory steeper than 20°.

5.2.2. Diameter Distribution as a Function of Azimuth

The secondary crater mean diameter does not show the same relationships with azimuth as does crater density. Without considering the variation in different annuli, the mean diameters in azimuthal bins from northeast to southeast are smaller than the rest of the area on average, but the difference is not as large as density (Figure 13). The mean diameter in section L1 is ~6.9 km, and the mean diameter of the following section is ~8.5 km (Figure 13). For the bins with a high density in the northwest, their mean diameters do not stand out (~ 9.2 km); instead, the bins with the very large mean diameters (~12.1 km in 25°–30°, ~11.1 km in 75°–80°) are low in density in some bars (Figure 13). Two factors may influence these results. (1) In the east, the distal area where craters are generally small is covered by mare deposits or the obscured/unmappable zone; and (2) small craters are more likely to be obscured in some regions because of the heterogeneity of target properties and postbasin formation processes.

On the other hand, the difference in mean diameters in different azimuthal ranges varies with distance. Comparing the mean diameters of secondary craters in sectors between 0.5 *R* and 1.5 *R* (Figure 10), where secondary craters are preserved and identified for the full azimuthal range, the mean diameters of the secondaries in the 40° to 140° azimuthal range are smaller than the other sectors in the same annulus. Those sectors with smaller mean crater diameters are located in the uprange direction of the impact. The smaller size of secondary craters in this direction indicates that the fragments ejected in the uprange are smaller on average than in other directions. Farther than a distance of 1.5 *R* from the Orientale rim crest, the sectors in 40° to 140° azimuthal range are flooded by mare and no secondary craters are recognized.

6. Size-Frequency Distribution

The cumulative SFD of Orientale secondary craters is shown in Figure 15. The very flat SFD for diameters less than 6 km might be due to a true lack of small secondaries, the potential incompleteness of the catalog of secondary craters, or the degradation of small craters so that they became unrecognizable.

Because of the inhomogeneity in the spatial distribution of secondaries, SFDs of Orientale secondaries in several specified regions are analyzed separately (Figure 15b). Those regions include (a) the annular area from Orientale rim to 2.5 *R* where the secondary chains were formed as continuous secondaries facies (Figure 8), (b) the annulus area from Orientale rim to 4 *R* that has the dominant identified secondaries (Figure 10), (c) the sector with azimuth angle ranges from 305° to 330° where the crater density is high (Figure 13), and (d) the sector within 4 *R* and azimuth angle from 305° to 330° where secondaries are the most concentrated. Results suggest that all four selected subregions have higher frequency than the entire secondary crater population, and region (d) has the highest frequency over the entire radial range (Figure 15b). For region

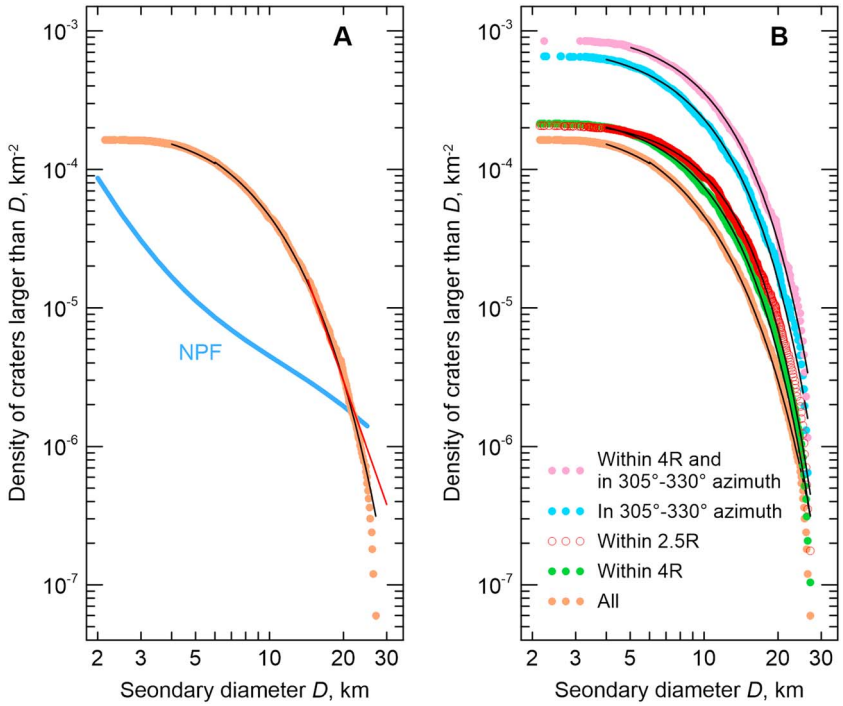

Figure 15. Cumulative size-frequency distribution of Orientale secondary craters. (a) SFD of all secondaries (orange dots), a power law fit for craters diameters $D > 14.3$ km (red line), and Weibull distribution fit (black line). Blue line ("NPF") shows model primary size-frequency distribution according to Neukum et al. (2001) for the assumed Orientale age of 3.8 Ga. (b) SFD of all Orientale secondary craters (the same as in a) and secondaries in different subregions; Weibull distribution fit (Table 2) for crater diameters >4–5 km from each subregion is shown with black lines. SFD = size-frequency distribution; NPF = Neukum production function.

(a) and (b), the frequencies overlap at diameters less than 5 km, but region (a) surpasses region (b) at greater diameters (Figure 15b).

In CSFD analysis, a best fit power law function is often used (e. g., Hirata & Nakamura, 2006; Wilhelms et al., 1978; Xiao et al., 2014). The form of the power law function is

$$N(\geq D) = A_1\ (D/1\ \mathrm{km})^{-b} \tag{9}$$

where $N(\geq D)$ is the cumulative number of secondary craters per square kilometer with diameter greater than or equal to D, b is the power law slope index, and A_1 is a constant factor. We applied the procedure by Clauset et al. (2009) to obtain simultaneous maximum likelihood estimate of the slope index b and the limiting diameter D_{min}, below which the power law approximation is not applicable. We obtained a steep slope, $b = 5.1$, and a large limiting diameter, $D_{min} = 14.3$ km, which means that the power law fits only the largest 10% of all secondaries. Table 2 shows the power law fit results for the separately analyzed regions.

Our results are consistent with previous studies of secondaries of smaller primaries (Hirata & Nakamura, 2006; Xiao, 2016), which found steep SFD of secondary crates ($b > 3$). However, that the power law (equation (9))

Table 2
Power law and Weibull Distribution Fits for Secondary Craters Size-Frequency Distributions in Different Regions

	Power law			Weibull distribution			
Region	D_{min} (km)	b	A_1 (km^{-2})	γ	D_W (km)	N_a (10^{-4} km^{-2})	D_M (km)
All secondaries	14.3	5.1	11	1.32	6.3	2.9	4.7
Annulus within 2.5 R	10.6	3.5	0.3	1.70	9.4	2.7	7.6
Annulus within 4 R	14.3	4.9	13	1.46	7.5	3.3	5.8
Sector with azimuth from 305° to 330°	14.3	5.0	53	1.36	7.1	11.0	5.4
Sector with azimuth from 305° to 330° within 4 R	14.3	4.8	57	1.57	8.8	11.9	7.0

describes the obtained SFD quite poorly: qualitatively, the SFD in the log-log plot (Figure 15a) is not similar to a straight line; quantitatively, the formal maximum likelihood procedure (Clauset et al., 2009) yields a power law fit only for a small part of the population only.

The fact that a power law does not describes secondary SFDs well has been discussed previously. Ivanov (2006) and Werner et al. (2009) suggested that a Weibull distribution may be a more appropriate description of the secondary CSFD:

$$N(\geq D) = N_a\{1-\exp[-(D/D_W)^{\gamma}]\} \tag{10}$$

where $\gamma > 1$ is the Weibull exponent, N_a is the total crater density, and D_W is the characteristic crater diameter: the distribution mode, mean, and median are proportional to D_W, in particular, the median diameter D_M is

$$D_M = D_W \ln(2)^{1/\gamma}. \tag{11}$$

Using data by Wilhelms et al. (1978) and assuming $\gamma = 2$, Ivanov (2006) obtained $D_W = 13$ km for Orientale secondaries, which corresponds to a median crater size of 10.8 km. We took advantage of our large data set and obtained the maximum likelihood estimation of both parameters, γ and D_W, simultaneously (e.g., Cohen, 1965) using only craters larger than 6 km, for which, we believe, our survey is more complete. We found that the Weibull distribution (equation (10)) fits the data well. Parameter estimation results for the whole population and its subsets are listed in Table 2, and fitted distributions are shown in Figure 15. Our values of the Weibull exponent are systematically lower than $\gamma = 2$ assumed by Ivanov (2006) and Werner et al. (2009), which indicates a relatively wider dispersion of crater diameters. The median crater diameters D_M derived from our fits are listed in Table 2; they turned out smaller than those deduced from the Ivanov (2006) fit.

The fitted Weibull distributions accurately reproduce the actual SFD down to $D \sim 4$ km (Figure 15), which suggests that our survey is complete down to this crater size. The number of craters smaller than 4 km in our data set is lower than predicted by the best fit Weibull distribution; the total number of "missing" small secondaries is ~42%. When we consider the subregions with denser and larger craters, the percentage of "missing" craters is even lower.

In Figure 15a we also compare densities of secondary and primary craters around the Orientale basin. Lacking the absolute age from samples, the age of Orientale basin is constrained to be between 3.85 and 3.72 Ga, and estimated to be 3.80 Ga from relative crater density (Wilhelms et al., 1987). Assuming this age and using the crater production function and chronology function by Neukum et al. (2001), we estimated the SFD of post-Orientale primary craters. It is shown in Figure 15a as "NPF" curve, "NPF" standing for the Neukum production function. Comparing the SFD of primary craters of Orientale age with Orientale secondary craters, we find that secondary craters are much more abundant than primary craters for diameters smaller than 20 km. This is consistent with the conclusions of Wilhelms et al. (1987).

7. Estimation of the Properties of Projectile Fragments that Produced Secondary Craters

Crater ejecta scaling laws provide a mechanism to estimate the size of impacting fragments from the crater size and the impactor velocity. For secondaries, fragment velocity can be derived from the distance of the secondary crater from the parent crater assuming a constant or known ejection angle (e.g., Oberbeck, 1975). The ejecta fragments that formed the identified Orientale secondaries are analyzed in this section to help understand the primary impact event initial conditions.

7.1. Estimation of Size of Ejecta Fragments

Assuming the ejection angle is 45° for all secondary craters (Hirata & Nakamura, 2006; Vickery, 1986, 1987), the velocity of fragments can be computed through equation (3). The ejection velocity versus distance is shown in Figure S1. Because it is impossible to locate the position within the expanding transient cavity from which a fragment was ejected, the distance is measured from the center of the Orientale basin. On the basis of the secondary crater distance range found in this study (Figure 6), the highest velocity is 1.8 km/s.

Collins et al. (2011) suggested a S index to quantify the ratio strength effect and gravity effect in cratering. Based on their method, S index of our data ranges from ~0.01 to ~0.24, indicating the cratering of the

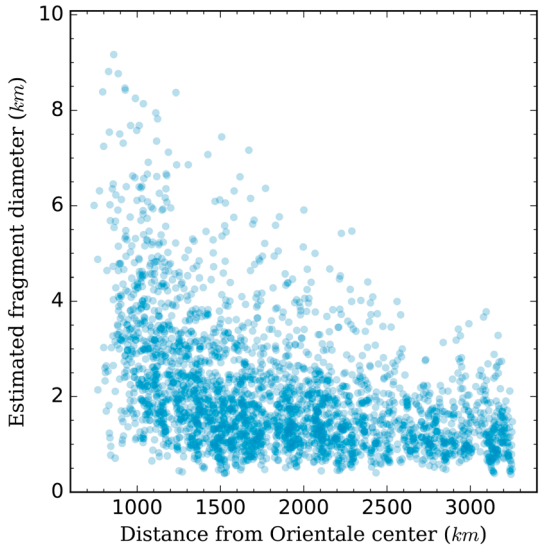

Figure 16. Ejecta fragment diameter distribution at different radial distances from the center of Orientale. Diameters are computed in gravity-dominated regime and with assuming that the incidence angle is 45°.

investigated secondaries belongs to gravity-dominated regime (Text S1 and Figure S2). Therefore, we can calculate the size of the impactors that formed the detected secondaries with equation (6) with ignoring the poorly constrained target yield strength. The distribution of fragment diameters with distance is shown in Figure 16. The largest fragment is ~9.2 km in diameter, and the smallest is ~0.4 km in diameter. The size of the largest fragments decreases with increasing distance, but most fragments are 0.5 to ~2 km in diameter at all distance ranges (Figure 16). Because the largest fragment diameters decrease, but the small fragment diameters are nearly constant, the size range of ejecta decreases with increasing radial distance from Orientale. This relationship of fragment size and radial distance is consistent with the findings of previous studies on smaller craters (Hirase et al., 2004; Hirata & Nakamura, 2006; Vickery, 1987). Because of the velocity variation of the fragments, the crater size formed by fragments with the same size but different velocity can be different in radius to about 1 km (Figure S3).

The size estimated for the largest fragments is ~10 km diameter, which is extremely large for a single fragment. Two factors may be responsible for these results. First, many secondary craters, especially larger ones, are likely to have been produced by the impact of clusters of fragments, rather than a single, large intact bedrock block (Schultz & Gault, 1984, 1985; Vickery, 1986; Xiao, 2016). In those cases, the estimated fragment size can be regarded as the equivalent size of the cluster of ejecta, and for some craters this can be demonstrated by the preserved shape of the crater rim (e.g., Schultz & Gault, 1984, 1985). Second, the diameter of secondaries may have been enlarged because of slumping of the wall (Herrick & Hessen, 2006).

There are two factors that probably affected the results of the calculated fragment size. One is that the ejection and incidence angle are both assumed to be 45°, which is a plausible assumption, but not likely to be the real scenario entirely (Vickery, 1986). If an ejecta fragment exceeds 45° ejection and impact incidence angle, then the real size is smaller than the diameter calculated for the 45° case. On the other hand, measuring the distance of the secondary crater position from the primary crater center will lead to overestimates of the fragment velocity and will underestimate the size of fragment (Vickery, 1987).

The Weibull distribution is widely used to describe rock fragmentation, and that theoretically predicted for failure-controlled disintegration (e.g., Brown & Wohletz, 1995). The overall distribution of the inferred ejecta fragment size follows a Weibull distribution with Weibull exponent $\gamma = 1.14$ and a characteristic fragment diameter of 1.6 km. This distribution is accurate down to a fragment diameter of 0.9 km; therefore, it comprises 88% of the fragment population by number, and only some fragments smaller than 0.9 km are "missing."

7.2. Spatial Distribution of the Volume of Ejecta Fragments

The spatial distribution of the volume of ejecta fragments can be estimated from the fragment diameters by assuming that all fragments are spherical. Figure 17 shows the distribution of the gross volume of fragments in annular sectors and their distribution after being normalized to sector area. For sectors at different radial distance, but the same azimuthal interval, the volume decreases with increasing distance (Figure 17). For example, taking the sectors in the azimuthal range 300°–320°, the normalized volume decreases gradually from 1 *R* to 6 *R*. This trend of decreasing volume with increasing distance does not change until 4.5–5 *R* as crater density, and the volume difference of sectors 0.5–1 *R* and 1–1.5 *R* is less than the discrepancy of crater density (Figures 10 and 17).

As shown in Figure 17, the volume distribution can be divided into four sections: (1) the large-volume region in the northwest, (2) the medium-volume region from the southeast to the southwest, (3) the wide small-volume region from the northeast to the southeast, and (4) the other narrow small-volume region in the southwest. The bilaterally symmetric pattern of the large-volume region and middle-volume region provides further supporting evidence for the proposed Orientale impact incidence direction.

The total volume of fragments estimated in this study is ~3.5×10^4 km^3. If we adopt the Outer Rook Mountains as an estimate of the largest extent of the transient cavity (Fassett et al., 2011), Orientale basin

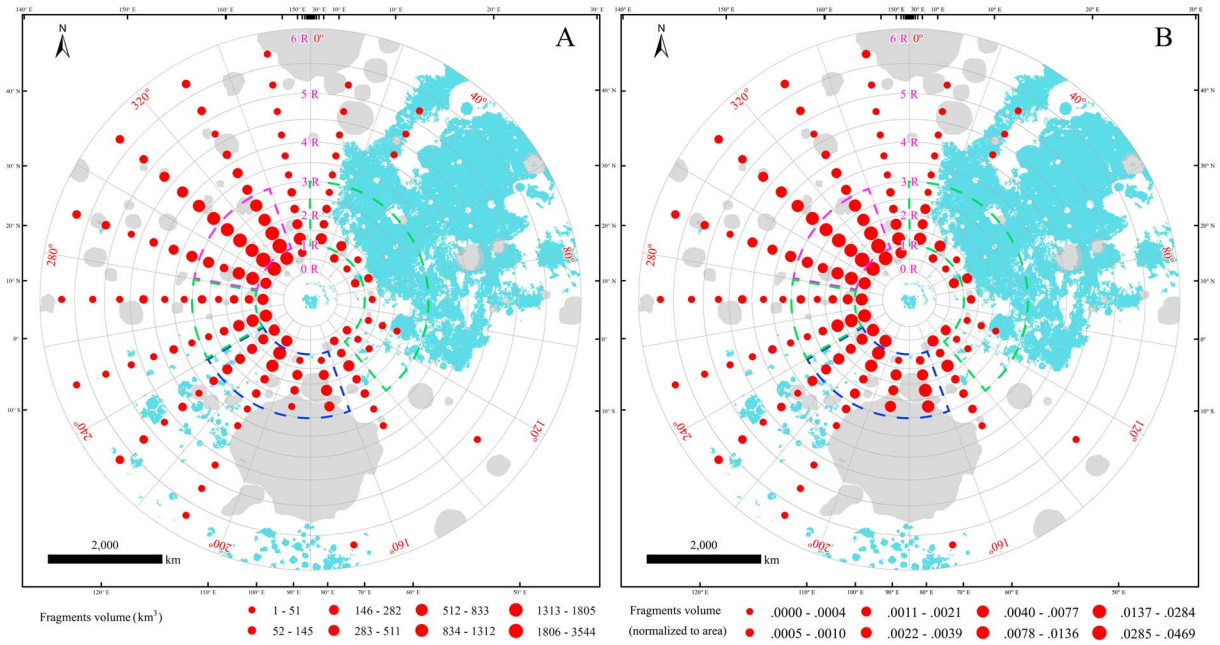

Figure 17. The gross volume of fragments in each annular sector (a) and the gross volume normalized to the area of the corresponding sector (b), denoted by red points. Within 1 *R* to 3 *R* radial range, the sector outlined with dashed purple line is the large-volume region; the medium-volume areas are outlined with dashed blue line; the small-volume regions are outlined with dashed green lines. The blue green shadow shows the coverage of maria; gray shadow shows the obscured/unmappable areas. The large-volume and medium-volume regions are approximately bilaterally symmetric to the azimuthal angle of ~240°–280°.

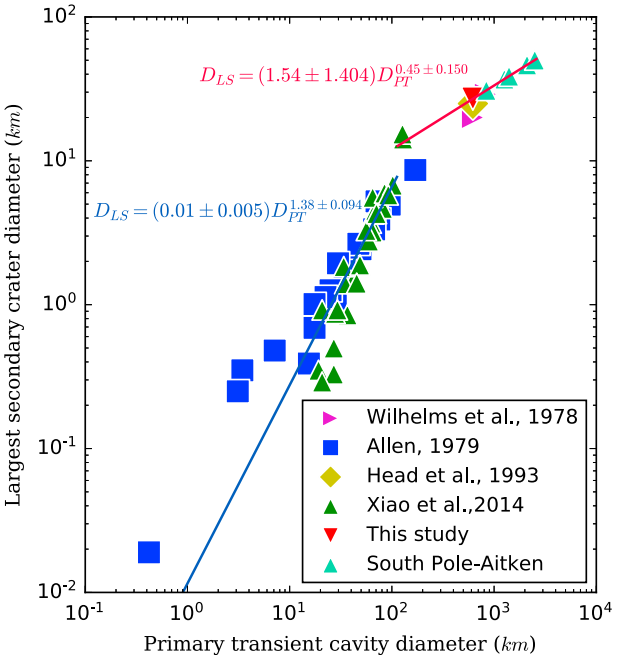

Figure 18. The largest secondary crater diameter versus transient cavity diameter of the parent crater and their power law fits. Power law fits are made separately for small primary craters and large primary craters. The transient cavity diameter of the South Pole-Aitken basin ranges from 840 km to 2,500 km, corresponding to a diameter range of the largest secondary crater from 30.9 km to 50.2 km.

impact would have excavated ~7.5 × 10^6 km^3 of material in total, and the ejecta volume from the Outer Rook Mountains to the Cordillera Mountains would be ~1.9 × 10^6 km^3 (Fassett et al., 2011). The projectile fragments that created the secondaries identified in this analysis occupy a very small part (~0.6%) of the total ejecta deposit emplaced beyond the Cordillera Mountains. If the transient crater diameter is ~390 km as suggested from GRAIL study, the ejecta that avoided collapsing into the crater is 4.2 × 10^6 km^3 (Johnson et al., 2016). In this case, the fragments occupy only 0.8% of the total ejecta.

8. The Largest Secondary Crater Size Versus Primary Crater Size

Several previous studies of secondary craters have provided data about the largest secondary craters observed on the Moon, as shown in Figure 18 (Allen, 1979; Head et al., 1993; Wilhelms et al., 1978; Xiao et al., 2014). Wilhelms et al. (1978) assessed the largest secondary craters associated with the Orientale and Imbrium basins by mapping subareas of their secondary crater fields. They found that among 569 secondaries measured for the Orientale basin, the largest secondary crater was ~20 km in diameter; their study area, however, occupied only 1.75 × 10^6 km^2. For the Imbrium basin, among 2,080 secondaries measured in a larger area (4.17 × 10^6 km^2), they found that the largest secondary crater was ~29 km. Allen (1979) investigated the secondaries of 19 primary craters with diameters ranging from 0.5 km to 260 km, and the largest diameter of secondaries for a primary crater was given by the average diameter of five largest secondary craters associated with the parent crater. Results show that the mean largest secondary diameter is nearly linearly proportional to primary diameter in logarithmic coordinates.

Another estimate of the largest diameter of secondary crater for the Orientale basin is 25 km, measured using Galileo data (Head et al., 1993). To compare fresh complex impact craters on Mercury and the Moon, Xiao et al. (2014) investigated secondary craters of 17 lunar craters 20–190 km in diameter that formed in a highland substrate and 10 craters 20–90 km in diameter that formed in mare regions. The largest diameters of secondaries versus diameters of primary craters have very close slopes on mare and highland regions, indicating that terrain type does not affect the range of secondary crater diameters (Xiao et al., 2014).

To obtain a relationship between the diameter of the largest secondary (D_{LS}) and the size of their parent craters, the transient crater diameters (D_{PT}) of their primaries are estimated. The transient crater diameter for simple craters (smaller than 15 km) is calculated using equation $D_{PT} = 0.84D$ from Melosh (1989), and for complex craters (larger than 15 km) it is calculated using equation $D_{PT} = D_Q{}^{0.15}D^{0.85}$ (D_Q = 15 km) from Croft (1985). The transient crater diameter for the Orientale basin is assumed to be 390 km (Johnson et al., 2016). The adopted Imbrium basin transient diameter is 830 km, as suggested by Schultz and Crawford (2016), in their high speed (25 km/s) scenario.

The ratio of the largest secondary crater diameter (D_{LS}) to the parent transient cavity diameter (D_{PT}) decreases with increasing primary diameter. In log(D_{LS})-log(D_{PT}) space, the data for the largest secondary diameter versus parent transient diameter is clearly separated into two trends with different slopes (Figure 18). The first group is small primary craters, which have a higher slope (higher power law exponent); the second group is large primary craters, with a lower slope (lower power law exponent). To describe the relationship of D_{LS} and D_{PT} in the different diameter ranges, two power law equations are fitted from small craters and large craters respectively (Figure 18). The equation from the small crater group, which includes craters less than 180 km in diameter (Allen, 1979; Xiao et al., 2014), is $D_{LS} = (0.01\pm0.005)D_{PT}^{1.38\pm0.094}$. The crater data used to fit the power law equation for large primary craters include Tsiolkovskiy (Xiao et al., 2014, D_{PT} = 126.9 km) and Petavius (Xiao et al., 2014, D_{PT} = 128.7 km), Iridum crater (Allen, 1979, D_{PT} = 169.5 km), Orientale basin (from this study), and the Imbrium basin (Schultz & Crawford, 2016; Wilhelms et al., 1978). The relationship of D_{LS} and D_{PT} for large craters is $D_{LS} = (1.54\pm1.404)D_{PT}^{0.45\pm0.150}$.

The SPA basin is the oldest and largest confirmed impact basin on the Moon. Its ejecta deposit is the basic rock-stratigraphic unit associated with the SPA impact event (Guo et al., 2016). The original ejecta deposits, however, are difficult to recognize because of the great age of the basin and the significant subsequent degradation of its ejecta deposits and secondary craters. The relationship of secondary craters to ejecta fragments provides evidence for ejecta emplacement, and if they can be recognized, the secondaries of the SPA basin can be regarded as components of SPA ejecta stratigraphy. Based on the primary/secondary size relationship function derived above, the largest diameter of SPA secondaries can be estimated from its transient crater diameter. The SPA transient crater diameter has been estimated by numerous workers, and there is a wide range of reported values; these include 2,500 km (Hammond et al., 2009), 2100 km (Wieczorek & Phillips, 1999), 1,400 km (Spudis, 1993), 1260 km (Petro & Pieters, 2002), and 840 km diameter (Potter et al., 2012). Therefore, the corresponding diameter of the largest secondary crater could range from ~30 to 50 km (50.2 km, 46.4 km, 38.8 km, 37.0 km and 30.9 km respectively, as shown in Figure 18). The study of Garrick-Bethell and Zuber (2009) shows that the major axis of the SPA outer ring is ~2,400 km, which indicates the 2,500 km transient diameter estimate is likely to be too large, and that the 2,100 km transient diameter may also be unreasonable. Based on these analyses, we infer that the largest secondary crater of the SPA basin is not likely to be larger than ~40 km. The relationships derived from the largest secondary crater diameter and final diameter of the primary crater also suggest ~40 km in diameter for the largest secondary crater of the SPA basin (Figure S5). Given the fact that the SPA basin is the largest known impact basin on the Moon, the estimated ~40 km SPA secondary crater diameter would represent the largest secondary craters produced on the Moon.

9. Conclusions

We identified 2,728 secondary craters associated with the Orientale basin within six radii from the ~920 km diameter Montes Cordillera Ring. Analysis of their spatial distribution reveals the density and diameter relationships of the secondary craters with azimuth and distance from the primary Orientale basin. Orientale secondary craters are concentrated in an annular area with radial distance ranges from 1 *R* to 3.5

R, which includes much of the continuous secondary crater facies, where secondary chains were formed. The highest crater numbers and densities are in annuli from 1 *R* to 2.5 *R*. The number and density of secondary craters in more distal regions is low; this may be due in part to the difficulty of distinguishing secondary craters from primary craters at great distances from the parent crater. Secondary crater mean diameter and maximum diameter increase as radial distance increases, while the minimum diameter is nearly constant with distance, probably due to the difficulty of recognizing the smallest secondary craters. The distribution of secondaries in the most proximal annuli (within 1.5 *R*) on the eastern side of Orientale suggests that the low crater density observed in that sector in general is not caused solely by post-Orientale mare flooding. The densities of secondaries in different azimuthal sectors indicate that the Orientale impact downrange direction was between the azimuth of 240° to 265°, and the incidence angle was steeper than 20° with considering the ellipticity of the Orientale basin. The mean secondary crater diameter does not show a close relationship with azimuth, but the azimuth range in 40°–140° has a relatively smaller mean diameter.

The cumulative secondary CSFD does not have a constant power law slope in the diameter range of detected secondaries; its slope steepens as the diameter increases, and the CSFDs for four specific regions have a similar slope trend. The distributions for craters larger than 4 km are well fitted by a Weibull distribution with exponents between 1.3 and 1.7. For smaller craters, the observed distributions are flatter than the Weibull distribution, possibly due to the difficulty of confidently recognizing of small secondary craters, and their enhanced degradation.

Using a crater ejecta scaling relationship, the size of fragments that formed the secondaries identified in this study was estimated. The largest (~10-km diameter) is probably the size equivalent of tight clusters of ejecta, not one individual fragment. The size of the largest fragment decreases with increasing distance, but most fragments are 0.5~2 km in diameter over the entire distance range. The fragment volume distribution shows that the volume decreases with increasing distance. The fragment volume distribution with azimuth is consistent with the proposed impact direction and incidence angle derived from the distribution of secondary craters. The total fragment volume sums to ~3.5×10^4 km^3, which is only ~0.6% of the entire volume of ejecta deposited in the area beyond Cordillera Mountains.

Ejecta from both the SPA basin and the Orientale basin contributed significant material to the megaregolith, and they are superposed in a broad area. Projectiles that formed the secondary craters, although small in relation to the entire ejecta volume, played an important role in forming signatures of these impact events. Abundant Orientale secondary craters are recognized in the interior region of the SPA basin. The appearance of secondary craters in the SPA basin suggests that sample return missions to the SPA basin could sample and date both the youngest and oldest major lunar basins. If scaling the distance range of the highest secondary crater density of the Orientale basin to SPA basin, the secondaries of SPA basin are more likely to be detected in the radial range of 2,200 km to 5,500 km from SPA rim. In this case, the secondary craters of SPA basin are concentrated in the opposite hemisphere.

Based on the relationship of diameters of the largest secondary crater and the parent crater from this study and from several other large primary craters, the estimated diameter of the largest secondary crater of the SPA basin is ~40 km, the largest secondaries that are likely to exist on the Moon. The recognition of chains, clusters, or individual craters of this size may be an important technique to help utilize the SPA basin event as a stratigraphic marker.

Acknowledgments
We deeply grateful to the LOLA and LROC team of the NASA Lunar Reconnaissance Orbiter Mission and NASA's Planetary Data System (PDS) for providing the data to undertake and complete our study. We also acknowledge the SELENE mission and the JAXA SELENE Data Archive. The secondary crater catalog is accessible at http://www.planetary.brown.edu/html_pages/data.htm and in the supporting information. This study is supported by the Strategic Priority Research Program (B) of Chinese Academy of Sciences (grant XDB18000000), the National Key Basic Research Special Foundation of China (grant 2015FY210500), the National Natural Science Foundation of China (grants 41773065, 41490634, and 41373068), and the Key Program of Frontier Science of Chinese Academy of Sciences (grant QYZDY-SSW-DQC028). We gratefully acknowledge funding from Brown University, Office of Vice President, for Research SEED grant "Engaging the Chinese Lunar Exploration Program (CLEP)." We gratefully acknowledge very detailed and helpful reviews by Zhiyong Xiao, an anonymous reviewer, and Associate Editor Gareth Collins.

References

Allen, C. C. (1979). Large lunar secondary craters: Size-range relationships. *Geophysical Research Letters*, *6*, 51–54. https://doi.org/10.1029/GL006i001p00051

Anderson, J. L. B., Schultz, P. H., & Heineck, J. T. (2003). Asymmetry of ejecta flow during oblique impacts using three-dimensional particle image velocimetry. *Journal of Geophysical Research*, *108*(E8), 5094. https://doi.org/10.1029/2003JE002075

Arvidson, R. E., Boyce, J., Chapman, C., Cintala, M., Fulchignoni, M., Moore, H., et al. (1979). Standard techniques for presentation and analysis of crater size-frequency data. *Icarus*, *37*(2), 467–474.

Bierhaus, E. B., Chapman, C. R., & Merline, W. J. (2005). Secondary craters on Europa and implications for cratered surfaces. *Nature*, *437*(7062), 1125–1127. https://doi.org/10.1038/nature04069

Bierhaus, E. B., Chapman, C. R., Merline, W. J., Brooks, S. M., & Asphaug, E. (2001). Pwyll secondaries and other small craters on Europa. *Icarus*, *153*(2), 264–276. https://doi.org/10.1006/icar.2001.6690

Bottke, W. F., Love, S. G., Tytell, D., & Glotch, T. (2000). Interpreting the elliptical crater populations on Mars, Venus, and the Moon. *Icarus*, *145*(1), 108–121. https://doi.org/10.1006/icar.1999.6323

Brown, W. K., & Wohletz, K. H. (1995). Derivation of the Weibull distribution based on physical principles and its connection to the Rosin-Rammler and lognormal distributions. *Journal of Applied Physics*, *78*(4), 2758–2763. https://doi.org/10.1063/1.360073

Clauset, A., Shalizi, C. R., & Newman, M. E. J. (2009). Power-law distributions in empirical data. *SIAM Review*, *51*(4), 661–703. https://doi.org/10.1137/070710111

Cohen, A. C. (1965). Maximum likelihood estimation in the Weibull distribution based on complete and on censored samples. *Technometrics*, *7*(4), 579–588. https://doi.org/10.2307/1266397

Collins, G. S., Elbeshausen, D., Davison, T. M., Robbins, S. J., & Hynek, B. M. (2011). The size-frequency distribution of elliptical impact craters. *Earth and Planetary Science Letters*, *310*(1–2), 1–8. https://doi.org/10.1016/j.epsl.2011.07.023

Croft, S. K. (1985). The scaling of complex craters. *Journal of Geophysical Research*, *90*(S02), C828–C842. https://doi.org/10.1029/JB090iS02p0C828

Davison, T. M., Collins, G. S., Elbeshausen, D., Wunnemann, K., & Kearsley, A. (2011). Numerical modeling of oblique hypervelocity impacts on strong ductile targets. *Meteoritics & Planetary Science*, *46*(10), 1510–1524. https://doi.org/10.1111/j.1945-5100.2011.01246.x

Evans, A. J., Soderblom, J. M., Andrews-Hanna, J. C., Solomon, S. C., & Zuber, M. T. (2016). Identification of buried lunar impact craters from GRAIL data and implications for the nearside maria. *Geophysical Research Letters*, *43*, 2445–2455. https://doi.org/10.1002/2015GL067394

Fassett, C. I., Head, J. W., Smith, D. E., Zuber, M. T., & Neumann, G. A. (2011). Thickness of proximal ejecta from the Orientale Basin from Lunar Orbiter Laser Altimeter (LOLA) data: Implications for multi-ring basin formation. *Geophysical Research Letters*, *38*, L17201. https://doi.org/10.1029/2011GL048502

Garrick-Bethell, I., & Zuber, M. T. (2009). Elliptical structure of the lunar South Pole-Aitken basin. *Icarus*, *204*(2), 399–408. https://doi.org/10.1016/j.icarus.2009.05.032

Gault, D. E., & Wedekind, J. A. (1978). Experimental studies of oblique impact, Lunar and Planetary Science Conference, 9. (pp. 3843–3875). Houston, TX.

Guo, D., Liu, J., Sun, Y., Ji, J., Liu, J., Wang, J., et al. (2016). A lunar time scale from geodynamic evolution perspective, Lunar and Planetary Science Conference, 47. (pp. 1744). Houston, TX.

Hammond, N. P., Nimmo, F., & Korycansky, D. G. (2009). Hydrocode modelling of the South Pole-Aitken basin-forming impact, Lunar and Planetary Science Conference, 40. (pp. 1455). Houston, TX.

Hartmann, W. K. (1970). Lunar cratering chronology. *Icarus*, *13*(2), 299–301. https://doi.org/10.1016/0019-1035(70)90059-X

Hartmann, W. K., & Kuiper, G. P. (1962). Concentric structures surrounding lunar basins. *Communications of the Lunar and Planetary and Laboratory*, *1*, 51–66.

Hartmann, W. K., & Wood, C. A. (1971). Moon: Origin and evolution of multi-ring basins. *The Moon*, *3*(1), 3–78. https://doi.org/10.1007/BF00620390

Haruyama, J., Matsunaga, T., Ohtake, M., Morota, T., Honda, C., Yokota, Y., et al. (2008). Global lunar-surface mapping experiment using the Lunar Imager/Spectrometer on SELENE. *Earth, Planets and Space*, *60*(4), 243–255. https://doi.org/10.1186/BF03352788

Head, J. (1977). Origin of outer rings in lunar multi-ringed basins-Evidence from morphology and ring spacing. In *Impact and explosion cratering: Planetary and terrestrial implications; Proceedings of the Symposium on Planetary Cratering* (pp. 563–573). New York, Pergamon Press, Flagstaff, Ariz.

Head, J. W. (1974). Orientale multi-ringed basin interior and implications for the petrogenesis of lunar highland samples. *The Moon*, *11*(3–4), 327–356. https://doi.org/10.1007/BF00589168

Head, J. W., Murchie, S., Mustard, J. F., Pieters, C. M., Neukum, G., Mcewen, A., et al. (1993). Lunar impact basins: New data for the western limb and far side (Orientale and South-Pole Aitken Basins) from the 1st Galileo flyby. *Journal of Geophysical Research*, *98*(E9), 17,149–17,181. https://doi.org/10.1029/93JE01278

Head, J. W., & Wilson, L. (2017). Generation, ascent and eruption of magma on the Moon: New insights into source depths, magma supply, intrusions and effusive/explosive eruptions (Part 2: Predicted emplacement processes and observations). *Icarus*, *283*, 176–223. https://doi.org/10.1016/j.icarus.2016.05.031

Herrick, R. R., & Forsberg-Taylor, N. K. (2003). The shape and appearance of craters formed by oblique impact on the Moon and Venus. *Meteoritics & Planetary Science*, *38*(11), 1551–1578. https://doi.org/10.1111/j.1945-5100.2003.tb00001.x

Herrick, R. R., & Hessen, K. K. (2006). The planforms of low-angle impact craters in the northern hemisphere of Mars. *Meteoritics & Planetary Science*, *41*(10), 1483–1495. https://doi.org/10.1111/j.1945-5100.2006.tb00431.x

Hirase, Y., Nakamura, A. M., & Michikami, T. (2004). Ejecta size-velocity relation derived from the distribution of the secondary craters of kilometer-sized craters on Mars. *Planetary and Space Science*, *52*(12), 1103–1108. https://doi.org/10.1016/j.pss.2004.07.007

Hirata, N., & Nakamura, A. M. (2006). Secondary craters of Tycho: Size-frequency distributions and estimated fragment size-velocity relationships. *Journal of Geophysical Research*, *111*, E03005. https://doi.org/10.1029/2005JE002484

Holsapple, K. A. (1993). The scaling of impact processes in planetary sciences. *Annual Review of Earth and Planetary Sciences*, *21*(1), 333–373. https://doi.org/10.1146/annurev.earth.21.1.333

Holsapple, K. A., & Housen, K. R. (2007). A crater and its ejecta: An interpretation of deep impact. *Icarus*, *187*(1), 345–356. https://doi.org/10.1016/j.icarus.2006.08.029

Huang, Q., & Wieczorek, M. A. (2012). Density and porosity of the lunar crust from gravity and topography. *Journal of Geophysical Research*, *117*, E05003. https://doi.org/10.1029/2012JE004062

Ivanov, B. A. (2006). Notes about secondary crater SFD, *Workshop on surface ages and histories: Issues in planetary chronology*, LPI Contribution No. 1320 (pp. 28–29). Houston, TX.

Ivanov, B. A., Neukum, G., & Wagner, R. (2001). Size-frequency distributions of planetary impact craters and asteroids. In M. Y. Marov & H. Rickman (Eds.), *Collisional processes in the solar system* (pp. 1–34). Netherlands: Kluwer Academic Publishers. https://doi.org/10.1007/978-94-010-0712-2_1

Johnson, B. C., Blair, D. M., Collins, G. S., Melosh, H. J., Freed, A. M., Taylor, G. J., et al. (2016). Formation of the Orientale lunar multiring basin. *Science*, *354*(6311), 441–444. https://doi.org/10.1126/science.aag0518

Liu, J., Liu, J., Guo, D., Ji, J., Wang, Q., & Li, S. (2016). Comprehensive analysis of the lunar Orientale Basin and research of the initial impact condition. *Acta Petrologica Sinica*, *32*(1), 135–143.

McCauley, J. F. (1977). Orientale and Caloris. *Physics of the Earth and Planetary Interiors*, *15*(2–3), 220–250. https://doi.org/10.1016/0031-9201(77)90033-4

McEwen, A. S., & Bierhaus, E. B. (2006). The importance of secondary cratering to age constraints on planetary surfaces. *Annual Review of Earth and Planetary Sciences*, *34*(1), 535–567. https://doi.org/10.1146/annurev.earth.34.031405.125018

McGill, G. E. (1977). Craters as "fossils": The remote dating of planetary surface materials. *Geological Society of America Bulletin*, *88*(8), 1102–1110. https://doi.org/10.1130/0016-7606(1977)88%3C1102:CAFTRD%3E2.0.CO;2

Melosh, H. J. (1989). Impact cratering: A geologic process. In *Oxford Monographs on Geology and Geophysics* (pp. 60–184). New York: Oxford University Press.

Michael, G. G., & Neukum, G. (2010). Planetary surface dating from crater size-frequency distribution measurements: Partial resurfacing events and statistical age uncertainty. *Earth and Planetary Science Letters*, *294*(3–4), 223–229. https://doi.org/10.1016/j.epsl.2009.12.041

Moore, H. J., Hodges, C. A., & Scott, D. H. (1974). Multiringed basins-illustrated by Orientale and associated features, 5th Lunar Science Conference (pp. 71–100). New York, Pergamon Press, Houston, TX.

Morse, Z. R., Osinski, G. R., & Tornabene, L. L. (2018). New morphological mapping and interpretation of ejecta deposits from Orientale Basin on the Moon. *Icarus*, *299*, 253–271. https://doi.org/10.1016/j.icarus.2017.08.010

Mottmann, J. (1977). Origin of late heavy bombardment. *Icarus*, *31*(3), 412–413. https://doi.org/10.1016/0019-1035(77)90032-X

Mustard, J. F., & Head, J. W. (1996). Buried stratigraphic relationships along the southwestern shores of Oceanus Procellarum: Implications for early lunar volcanism. *Journal of Geophysical Research*, *101*(E8), 18,913–18,925. https://doi.org/10.1029/96JE01826

Neukum, G., Ivanov, B. A., & Hartmann, W. K. (2001). Cratering records in the inner solar system in relation to the lunar reference system. *Space Science Reviews*, *96*(1/4), 55–86. https://doi.org/10.1023/A:1011989004263

Neukum, G., König, B., Fechtig, H., & Storzer, D. (1975). Cratering in the Earth-Moon system—Consequences for age determination by crater counting, Lunar Science Conference, 6. (pp. 2597–2620). Houston, TX.

Neumann, G. A., Zuber, M. T., Wieczorek, M. A., Head, J. W., Baker, D. M. H., Solomon, S. C., et al. (2015). Lunar impact basins revealed by Gravity Recovery and Interior Laboratory measurements. *Science Advances*, *1*(9), e1500852. https://doi.org/10.1126/sciadv.1500852

Oberbeck, V. R. (1975). The role of ballistic erosion and sedimentation in lunar stratigraphy. *Reviews of Geophysics*, *13*(2), 337–362. https://doi.org/10.1029/RG013i002p00337

Petro, N. E., & Pieters, C. M. (2002). The size and location of the transient crater of the South Pole-Aitken Basin, Lunar and Planetary Institute Science Conference, 33, 1848, Houston, TX.

Petro, N. E., & Pieters, C. M. (2008). The lunar-wide effects of basin ejecta distribution on the early megaregolith. *Meteoritics & Planetary Science*, *43*(9), 1517–1529. https://doi.org/10.1111/j.1945-5100.2008.tb01025.x

Pierazzo, E., & Melosh, H. J. (2000). Understanding oblique impacts from experiments, observations, and modeling. *Annual Review of Earth and Planetary Sciences*, *28*(1), 141–167. https://doi.org/10.1146/annurev.earth.28.1.141

Pike, R. J. (1972). Geometric similitude of lunar and terrestrial craters, International Geological Congress, 24. (pp. 41–47). Montreal, Canada.

Pike, R. J. (1974). Ejecta from large craters on the Moon: Comments on the geometric model of McGetchin et al. *Earth and Planetary Science Letters*, *23*(3), 265–271. https://doi.org/10.1016/0012-821X(74)90114-9

Pike, R. J., & Wilhelms, D. E. (1978). Secondary-impact craters on the Moon: Topographic form and geologic process, Lunar and Planetary Science Conference, 9, 907–909, Houston, TX.

Potter, R. W. K., Collins, G. S., Kiefer, W. S., McGovern, P. J., & Kring, D. A. (2012). Constraining the size of the South Pole-Aitken basin impact. *Icarus*, *220*(2), 730–743. https://doi.org/10.1016/j.icarus.2012.05.032

Potter, R. W. K., Kring, D. A., Collins, G. S., Kiefer, W. S., & McGovern, P. J. (2013). Numerical modeling of the formation and structure of the Orientale impact basin. *Journal of Geophysical Research: Planets*, *118*(5), 963–979. https://doi.org/10.1002/jgre.20080

Povilaitis, R. Z., Robinson, M. S., van der Bogert, C. H., Hiesinger, H., Meyer, H. M., & Ostrach, L. R. (2017). Crater density differences: Exploring regional resurfacing, secondary crater populations, and crater saturation equilibrium on the moon. *Planetary and Space Science*. https://doi.org/10.1016/j.pss.2017.05.006

Quantin, C., Popova, O., Hartmann, W. K., & Werner, S. C. (2016). Young Martian crater Gratteri and its secondary craters. *Journal of Geophysical Research: Planets*, *121*, 1118–1140. https://doi.org/10.1002/2015JE004864

Robbins, S. J., & Hynek, B. M. (2011). Secondary crater fields from 24 large primary craters on Mars: Insights into nearby secondary crater production. *Journal of Geophysical Research*, *116*, E10003. https://doi.org/10.1029/2011JE003820

Robbins, S. J., & Hynek, B. M. (2014). The secondary crater population of Mars. *Earth and Planetary Science Letters*, *400*, 66–76. https://doi.org/10.1016/j.epsl.2014.05.005

Robinson, M. S., Brylow, S. M., Tschimmel, M., Humm, D., Lawrence, S. J., Thomas, P. C., et al. (2010). Lunar Reconnaissance Orbiter Camera (LROC) instrument overview. *Space Science Reviews*, *150*(1–4), 81–124. https://doi.org/10.1007/s11214-010-9634-2

Schultz, P., & Gault, D. (1984). Effects of projectile deformation on cratering efficiency and morphology, Lunar and Planetary Science Conference, 15. (pp. 730–731). Houston, TX.

Schultz, P., & Papamarcos, S. (2010). Evolving flowfields from Imbrium and Orientale impacts, Lunar and Planetary Science Conference, 41, 2480, Houston, TX.

Schultz, P. H., & Crawford, D. A. (2016). Origin and implications of non-radial Imbrium Sculpture on the Moon. *Nature*, *535*(7612), 391–394. https://doi.org/10.1038/nature18278

Schultz, P. H., Eberhardy, C. A., Ernst, C. M., A'Hearn, M. F., Sunshine, J. M., & Lisse, C. M. (2007). The deep impact oblique impact cratering experiment. *Icarus*, *190*(2), 295–333. https://doi.org/10.1016/j.icarus.2007.06.006

Schultz, P. H., & Gault, D. E. (1985). Clustered impacts: Experiments and implications. *Journal of Geophysical Research*, *90*(B5), 3701–3732. https://doi.org/10.1029/JB090iB05p03701

Schultz, P. H., & Singer, J. (1980). A comparison of secondary craters on the Moon, Mercury, and Mars, Lunar and Planetary Science Conference, 11. (pp. 2243–2259). Houston, TX.

Scott, D. H., & McCauley, J. F. (1977). Geologic map of the west side of the Moon, 1:5 000 000, Geologic Atlas of the Moon, I-1034, US Geological Survey, Flagstaff, AZ.

Shoemaker, E. M. (1962). Interpretation of lunar craters. In Z. Kopal (Ed.), *Physics and astronomy of the Moon* (pp. 283–359). London: Academic Press.

Shoemaker, E. M. (1965). Preliminary analysis of the fine structure of the lunar surface in Mare Cognitum, JPL Tech. Report No. 32–700. In W. N. Hess, D. H. Menzel, & J. A. O'Keefe (Eds.), *The Nature of the Lunar Surface* (pp. 23–77). Baltimore, MD: Johns Hopkins Press. https://doi.org/10.1017/S0252921100115714

Shoemaker, E. M., Batson, R. M., Holt, H. E., Morris, E. C., Rennilson, J. J., & Whitaker, E. A. (1969). Observations of the lunar regolith and the Earth from the television camera on Surveyor 7. *Journal of Geophysical Research*, *74*(25), 6081–6119. https://doi.org/10.1029/JB074i025p06081

Shuvalov, V. (2011). Ejecta deposition after oblique impacts: An influence of impact scale. *Meteoritics & Planetary Science*, *46*(11), 1713–1718. https://doi.org/10.1111/j.1945-5100.2011.01259.x

Smith, D. E., Zuber, M. T., Jackson, G. B., Cavanaugh, J. F., Neumann, G. A., Riris, H., et al. (2010). The Lunar Orbiter Laser Altimeter investigation on the Lunar Reconnaissance Orbiter mission. *Space Science Reviews*, *150*(1–4), 209–241. https://doi.org/10.1007/s11214-009-9512-y

Spudis, P. D. (1993). *The geology of multi-ring impact basins: The Moon and other planets*. Cambridge, UK: Cambridge University Press. https://doi.org/10.1017/CBO9780511564581

Spudis, P. D., Hawke, B. R., & Lucey, P. (1984). Composition of Orientale basin deposits and implications for the lunar basin-forming process. *Journal of Geophysical Research*, *89*(S01), C197–C210. https://doi.org/10.1029/JB089iS01p0C197

Strom, R. G., Malhotra, R., Xiao, Z. Y., Ito, T., Yoshida, F., & Ostrach, L. R. (2015). The inner solar system cratering record and the evolution of impactor populations. *Research in Astronomy and Astrophysics*, *15*(3), 407–434. https://doi.org/10.1088/1674-4527/15/3/009

Tera, F., A, P. D., & J, W. G. (1974). Isotopic evidence for a terminal lunar cataclysm. *Earth and Planetary Science Letters*, *22*(1), 1–21. https://doi.org/10.1016/0012-821x(74)90059-4

van der Bogert, C. H., Hiesinger, H., Dundas, C. M., Krüger, T., McEwen, A. S., Zanetti, M., & Robinson, M. S. (2017). Origin of discrepancies between crater size-frequency distributions of coeval lunar geologic units via target property contrasts. *Icarus*, *298*, 49–63. https://doi.org/10.1016/j.icarus.2016.11.040

Vaughan, W. M., Head, J. W., Wilson, L., & Hess, P. C. (2013). Geology and petrology of enormous volumes of impact melt on the Moon: A case study of the Orientale basin impact melt sea. *Icarus*, *223*(2), 749–765. https://doi.org/10.1016/j.icarus.2013.01.017

Vickery, A. M. (1986). Size-velocity distribution of large ejecta fragments. *Icarus*, *67*(2), 224–236. https://doi.org/10.1016/0019-1035(86)90105-3

Vickery, A. M. (1987). Variation in ejecta size with ejection velocity. *Geophysical Research Letters*, *14*, 726–729. https://doi.org/10.1029/GL014i007p00726

Werner, S. C., Ivanov, B. A., & Neukum, G. (2009). Theoretical analysis of secondary cratering on Mars and an image-based study on the Cerberus Plains. *Icarus*, *200*(2), 406–417. https://doi.org/10.1016/j.icarus.2008.10.011

Whitten, J., & Head, J. W. (2015). Lunar cryptomaria: Mineralogy and composition of ancient volcanic deposits. *Planetary and Space Science*, *106*, 67–81. https://doi.org/10.1016/j.pss.2014.11.027

Whitten, J., Head, J. W., Staid, M., Pieters, C. M., Mustard, J., Clark, R., et al. (2011). Lunar mare deposits associated with the Orientale impact basin: New insights into mineralogy, history, mode of emplacement, and relation to Orientale Basin evolution from Moon Mineralogy Mapper (M-3) data from Chandrayaan-1. *Journal of Geophysical Research*, *116*, E00G09. https://doi.org/10.1029/2010JE003736

Wieczorek, M. A., Neumann, G. A., Nimmo, F., Kiefer, W. S., Taylor, G. J., Melosh, H. J., et al. (2013). The crust of the Moon as seen by GRAIL. *Science*, *339*(6120), 671–675. https://doi.org/10.1126/science.1231530

Wieczorek, M. A., & Phillips, R. J. (1999). Lunar multiring basins and the cratering process. *Icarus*, *139*(2), 246–259. https://doi.org/10.1006/icar.1999.6102

Wilhelms, D. E. (1976). Secondary impact craters of lunar basins, Lunar and Planetary Science Conference, 7. (pp. 2883–2901). Houston, TX.

Wilhelms, D. E., McCauley, J. F., & Trask, N. J. (1987). *The geologic history of the Moon*, *USGS Professional Paper 1348* (pp. 1–281). Washington DC: US Government Printing Office.

Wilhelms, D. E., V. R. Oberbeck, & Aggarwal, H. R. (1978). Size-frequency distributions of primary and secondary lunar impact craters, Lunar and Planetary Science Conference, 9. (pp. 3735–3762). Houston, TX.

Wilson, L., & Head, J. W. (2017). Generation, ascent and eruption of magma on the Moon: New insights into source depths, magma supply, intrusions and effusive/explosive eruptions (Part 1: Theory). *Icarus*, *283*, 146–175. https://doi.org/10.1016/j.icarus.2015.12.039

Xiao, Z. Y. (2016). Size-frequency distribution of different secondary crater populations: 1. Equilibrium caused by secondary impacts. *Journal of Geophysical Research: Planets*, *121*, 2404–2425. https://doi.org/10.1002/2016JE005139

Xiao, Z. Y., & Strom, R. G. (2012). Problems determining relative and absolute ages using the small crater population. *Icarus*, *220*(1), 254–267. https://doi.org/10.1016/j.icarus.2012.05.012

Xiao, Z. Y., Strom, R. G., Chapman, C. R., Head, J. W., Klimczak, C., Ostrach, L. R., et al. (2014). Comparisons of fresh complex impact craters on Mercury and the Moon: Implications for controlling factors in impact excavation processes. *Icarus*, *228*, 260–275. https://doi.org/10.1016/j.icarus.2013.10.002

Xie, M., & Zhu, M.-H. (2016). Estimates of primary ejecta and local material for the Orientale basin: Implications for the formation and ballistic sedimentation of multi-ring basins. *Earth and Planetary Science Letters*, *440*, 71–80. https://doi.org/10.1016/j.epsl.2016.02.012

Yamamoto, S. (2002). Measurement of impact ejecta from regolith targets in oblique impacts. *Icarus*, *158*(1), 87–97. https://doi.org/10.1006/icar.2002.6862

Zhou, S., Xiao, Z., & Zeng, Z. (2015). Impact craters with circular and isolated secondary craters on the continuous secondaries facies on the Moon. *Journal of Earth Science*, *26*(5), 740–745. https://doi.org/10.1007/s12583-015-0579-y

Zhu, M. H., Wunnemann, K., & Potter, R. W. K. (2015). Numerical modeling of the ejecta distribution and formation of the Orientale basin on the Moon. *Journal of Geophysical Research: Planets*, *120*, 2118–2134. https://doi.org/10.1002/2015JE004827